



Effect of solid flow above a subducting slab on water distribution and melting at convergent plate boundaries

Amandine-Marie Cagnioncle,¹ E. M. Parmentier,¹ and Linda T. Elkins-Tanton^{1,2}

Received 10 January 2007; revised 14 May 2007; accepted 29 May 2007; published 12 September 2007.

[1] Hydrous fluids derived by dehydration of the downgoing slab at convergent plate boundaries are thought to provoke wet melting in the wedge above the downgoing plate. We have investigated the distribution of hydrous fluid and subsequent melt in the wedge using two-dimensional models that include solid mantle flow and associated temperature distributions along with buoyant fluid migration and melting. Solid mantle flow deflects hydrous fluid from their buoyant vertical migration through the wedge. Melting therefore does not occur directly above the region where hydrous fluids are released from the slab. A melting front develops where hydrous fluids first encounter mantle material hot enough to melt. Wet melting is influenced by solid flow through the advection of fertile mantle material into the wet melting region and the removal of depleted material. The region of maximum melting occurs where the maximum flux of water from slab mineral dehydration reaches the wet melting region. The extent of melting (F) and melt production rates increase with increasing convergence rate and grain size due to increased temperatures along the melting front and to increased fractions of water reaching the melting front, respectively. The position of isotherms above the wet solidus varies with increasing slab dip and thereby also influences F and melt production rates. Applying the understanding of wet melting from this study to geochemical studies of the Aleutians may help elucidate the processes influencing fluid migration and melt production in that region. Estimates of the timescale of fluid migration, seismic velocity variation, and attenuation are also investigated.

Citation: Cagnioncle, A.-M., E. M. Parmentier, and L. T. Elkins-Tanton (2007), Effect of solid flow above a subducting slab on water distribution and melting at convergent plate boundaries, *J. Geophys. Res.*, 112, B09402, doi:10.1029/2007JB004934.

1. Introduction

[2] Convergent plate boundaries are sites of important chemical exchange between the Earth's surface and its interior. The extensive volcanism observed at such boundaries is a surface expression of this exchange. Understanding how arc lavas are generated and migrate to the surface can therefore yield a better insight in the processes which occur in the mantle wedge above a subducting plate. A significant component of arc magmas is the introduction of hydrous fluids into the mantle wedge through the dehydration of slab minerals [e.g., Pawley and Holloway, 1993; Schmidt and Poli, 1998]. A simple view, as expressed in Figure 1, is that the released water ascends vertically in the wedge, provoking melting of the surrounding mantle and forming volcanoes above the dehydration region [Grove *et al.*, 2003].

[3] Even though the role of fluids in melting the mantle wedge is widely accepted, fluid migration and melting

processes are not well understood. What is the fate of the water released by slab dehydration reactions? How is melting affected by solid flow? How much melt is present and what influences its distribution and its chemistry? What are typical timescales for magma transport? How is the distribution of hydrous fluids in the wedge reflected by seismic velocities and attenuation?

[4] Previous studies addressed fluid migration in a subduction zone geometry by using a corner flow solution of an incompressible fluid with constant viscosity to model mantle flow in the wedge [Spiegelman and McKenzie, 1987; Davies and Stevenson, 1992; Iwamori, 1998]. Melt flow was modeled by buoyant porous flow within a permeable, deformable mantle matrix. Spiegelman and McKenzie [1987] and Phipps Morgan [1987] used such a formulation to argue that mantle flow-induced pressure gradients may control melt migration, and hence magmatic distribution, at subduction zones. However, while solid flow-induced pressure gradients can focus melt, their magnitude may not be large enough to be a controlling factor as the magnitude of flow-induced pressure gradients is proportional to the solid viscosity. In their study, Spiegelman and McKenzie [1987] used a viscosity of 10^{21} Pa s. However, geophysical observables at subduction zones, such as topography and gravity or geoid anomalies, indicate that mantle viscosity may be several orders of magnitude lower than 10^{21} Pa s

¹Department of Geological Sciences, Brown University, Providence, Rhode Island, USA.

²Now at Department of Earth, Atmospheric and Planetary Sciences, Massachusetts Institute of Technology, Cambridge, Massachusetts, USA.

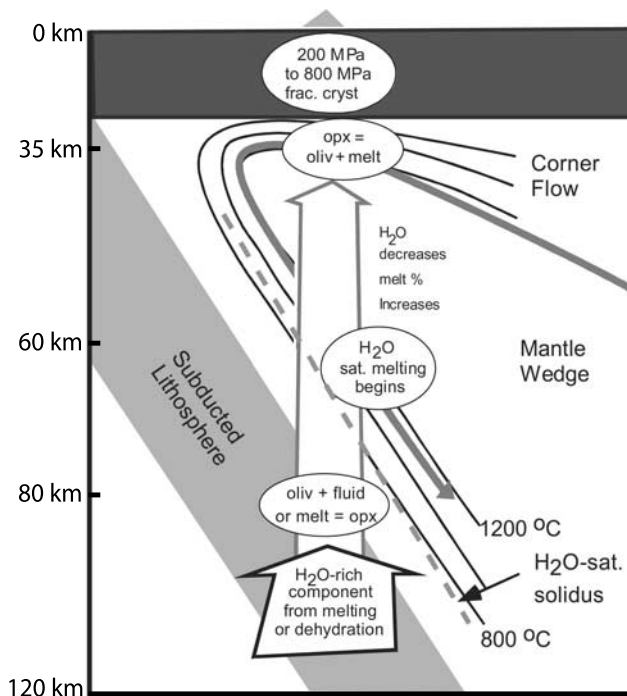


Figure 1. Conceptual model for melting in the mantle wedge above a subducting slab (modified from *Grove et al.* [2003] with kind permission from Springer Science and Business Media). Hydrous fluids released by dehydration in the slab rise buoyantly inducing wet melting in hot overlying mantle.

[Billen and Gurnis, 2001]. This low viscosity in the mantle wedge, perhaps due to the presence of high concentrations of water in the mantle above the slab [Hirth and Kohlstedt, 2003], could drastically reduce the effect of flow-induced pressure gradients. Therefore relative to the solid, melt percolates upward due to the buoyancy force rather than along directions of solid flow-induced pressure gradients. The absolute velocity of the melt is the vector sum of its vertical velocity through pores and the velocity of the solid within which it resides. A major goal of this study is to better understand the role of solid flow in the mantle wedge on fluid migration and melting.

[5] The location and extent of melting is controlled in part by the amount of water released by slab dehydration reactions that reaches a region in the wedge hot enough to melt. Temperature distributions derived from isoviscous mantle flow models [Davies and Stevenson, 1992; Iwamori, 1998] predict low enough temperatures that hydrous phases could be stable in significant portions of the mantle wedge. Davies and Stevenson [1992] thus argued that water released by the slab would be carried by amphibole in the mantle. As amphibole breaks down, water was envisioned to migrate over a significant horizontal distance to a hotter potential melting region. Recent studies [Schmidt and Poli, 1998] have however showed that amphibole is only stable to 2 GPa and that serpentine and chlorite cannot only hold more water than amphibole but are also stable to greater depth adjacent to the top of the slab [Pawley, 2003; Grove et al., 2006]. Iwamori [1998] presented numerical models in which the water released by slab dehydration reactions was

incorporated into mantle serpentine and chlorite. In these models, hydrous phases break down at about 150 km, releasing the water and causing melting once the wet solidus of peridotite is reached.

[6] Recent studies [Eberle et al., 2002; van Keken et al., 2002; Conder et al., 2002; Kelemen et al., 2003a] show that incorporating temperature- or/and stress-dependent rheology predicts significantly higher temperatures in the wedge than isoviscous rheology. Temperature-dependent viscosity enhances the entrainment of cooler, more viscous mantle just above the slab, creating higher mantle flow velocities in the wedge and causing hot mantle material to rise from greater depth toward the wedge corner. This flow pattern allows for less conductive cooling in the mantle wedge, leading to significantly higher temperatures in the wedge and along the slab top than those predicted for purely isoviscous flow at the same slab dip and convergence rate. The increased wedge and slab temperatures in turn thin the thermal boundary layer at the top of the slab and limit the occurrence of serpentine in the mantle above the slab. A greater amount of hydrous fluids than previously estimated is thereby released into the wedge by dehydration reactions in the slab.

[7] In this study, we used the estimates of water released by crustal dehydration of Schmidt and Poli [1998] and the thermal models of Kelemen et al. [2003a] to formulate two-dimensional (2-D) models of buoyant fluid migration and melting at subduction zones. Several previous studies have examined buoyant fluid migration and mantle flow. In an early study, Marsh [1979] suggested that melting occurred along the slab top and that the resulting melt rose in the form of three-dimensional diapiric flow. Wiggins and Spiegelman [1995] looked at the potential contribution to mantle magmatism of 3-D solitary waves migrating in a permeable and viscously deformable matrix. Honda and Yoshida [2005] considered the three-dimensional structure of thermal convection in the mantle wedge driven by instability of the cold thermal boundary layer at the base of the lithosphere. They associated the along-strike melt distribution in the wedge with the resulting thermal distribution. In this study, we assume that the distribution of hydrous fluids and melt is simply uniform in the along-arc direction. Future studies will look at the potentially important three-dimensional effects of melt localization above the region of wet melting.

[8] We find that solid mantle flow impacts the location of melting, melt production rates and the subsequent distribution of melt in the wedge. Wet melting in the wedge is mostly limited to a narrow front where hydrous fluids first encounter mantle material which is hot enough to melt. Since solid flow prevents water from rising vertically into the wedge, wet melting does not necessarily occur directly above the region of water release from the slab. Even though a broader potential melting region is present at high convergence rate due to overall higher wedge temperatures, the melt production rate is limited by the flux of water and fertile mantle material through that melting front. Indeed, the magnitude of solid flow increases with increasing convergence rate, thereby advecting a greater fraction of released hydrous fluids to greater depths. This fraction of hydrous fluids does not induce wet melting and hence restricts the amount of melt produced. The subsequent

distributing of melt within the wedge is also influenced by the increased magnitude of solid flow: A broader distribution of magma is observed with increasing convergence rates.

[9] We will first describe the formulation of our models and then analyze the resulting fluid distributions in terms of solid flow, distribution of water release along the top of the slab, thermal distribution, grain size distribution and slab dip. The model predictions will then be compared to geochemical and seismic constraints.

2. Model Formulation

[10] Numerous earlier studies have treated the migration of melt through mantle rock deforming by thermally activated creep as the flow of a fluid through a permeable, compacting viscous solid [Sleep, 1974; Ahern and Turcotte, 1979; McKenzie, 1984; Scott and Stevenson, 1984; Spiegelman, 1993]. Here we are interested in understanding how the fluid and solid interact chemically as melting transfers components from the solid to the fluid (melt) phase. Conservation of the total constituents in a representative volume element containing both solid and fluid (melt + water) with a fluid volume fraction ϕ can be expressed as

$$\begin{aligned} \frac{\partial}{\partial t} \left[\left(N_{\text{SO}} + N_{\text{H}_2\text{O}}^{\text{solid}} \right) (1 - \phi) + \left(N_{\text{H}_2\text{O}}^{\text{fluid}} + N_{\text{DO}} \right) \phi \right] \\ = -\nabla \cdot \left[\mathbf{V}_{\text{solid}} \left(N_{\text{SO}} + N_{\text{H}_2\text{O}}^{\text{solid}} \right) (1 - \phi) + \mathbf{V}_{\text{fluid}} \left(N_{\text{H}_2\text{O}}^{\text{fluid}} + N_{\text{DO}} \right) \phi \right] \end{aligned} \quad (1)$$

where ϕ is the volume fraction of melt or fluid, N_{SO} and $N_{\text{H}_2\text{O}}^{\text{solid}}$ are the number of moles of solid oxides and water, respectively, per unit volume of solid, and $\mathbf{V}_{\text{solid}}$ and $\mathbf{V}_{\text{fluid}}$ are the solid and fluid velocity, respectively. The composition of the melt is described by the number of moles of water and dissolved oxides other than water per unit volume, $N_{\text{H}_2\text{O}}^{\text{fluid}}$ and N_{DO} , respectively, that it contains. Melt will contain a number of dissolved oxides, depending on its temperature, pressure, and fluid content and on the composition of the solid phases with which the melt has equilibrated. In more complete models than those presented here, N_{SO} and N_{DO} values could be introduced for various oxide components both in the solid and in the melt using an algorithm such as MELTS [e.g., Hirschmann *et al.*, 1999; Asimow *et al.*, 2004; Baker *et al.*, 2004]. The simplifications of the present formulation can be relaxed in future models, but a first simple approach seems appropriate here.

[11] Water in the solid can be present in hydrous minerals, such as chlorite or serpentine, and can be dissolved in nominally anhydrous minerals. Water solubility in mantle minerals increases significantly with increasing temperature and pressure [Hirth and Kohlstedt, 2003; Bell *et al.*, 2003]. For the mantle wedge temperature distributions considered, hydrous minerals are not stable throughout most of the wedge but only in a thin region near the top of the slab. As discussed later, the effect of hydrous minerals will be mostly to control the distribution of water release into the anhydrous wedge. The models presented here take $N_{\text{H}_2\text{O}}^{\text{solid}} = 0$, but the potentially important effect of water dissolved in

nominally anhydrous minerals will need to be considered in future studies.

[12] In our models, water therefore only resides in the fluid phase where it is neither created nor destroyed. Conservation of water hence requires that

$$\frac{\partial}{\partial t} \left(N_{\text{H}_2\text{O}}^{\text{fluid}} \phi \right) = -\nabla \cdot \left(\mathbf{V}_{\text{fluid}} N_{\text{H}_2\text{O}}^{\text{fluid}} \phi \right) \quad (2)$$

where the product $N_{\text{H}_2\text{O}}^{\text{fluid}} \phi$ represents the number of moles of water per unit volume in a representative elemental volume. Since in our models water is present only in the fluid phase, the superscript fluid will be omitted in the remainder of this section.

[13] Dissolved oxides can either be advected in an elemental volume or be generated within that volume by melting, so

$$\frac{\partial}{\partial t} [N_{\text{DO}} \phi] = -\nabla \cdot [\mathbf{V}_{\text{fluid}} N_{\text{DO}} \phi] + \Gamma, \quad (3)$$

where Γ is the rate of melting, which is defined as the rate of transfer of solid oxides to the fluid phase, or

$$\Gamma = -\frac{\partial}{\partial t} [N_{\text{SO}} (1 - \phi)] - \nabla \cdot [\mathbf{V}_{\text{solid}} N_{\text{SO}} (1 - \phi)]. \quad (4)$$

[14] As a mantle parcel melts, it becomes depleted ($\xi > 0$, where ξ is the amount of melt that a given parcel of solid has already produced) and no longer able to produce additional melt at the same temperature, pressure and water content. More melting requires higher temperature, lower pressure, or increased water content. We consider this effect of solid depletion on melting by tracking the amount of melt ξ that a given parcel of solid has produced. Depleted solid is advected through the mantle wedge with the solid-state flow according to

$$\frac{\partial \xi}{\partial t} + \mathbf{V}_{\text{solid}} \cdot \nabla \xi = \Gamma. \quad (5)$$

[15] The relative proportion of water and dissolved oxides in the liquid phase depends on the extent of melting. The mole fraction of melt F is defined as

$$F = \frac{(N_{\text{H}_2\text{O}} + N_{\text{DO}}) \phi}{N_{\text{SO}} (1 - \phi) + (N_{\text{DO}} + N_{\text{H}_2\text{O}}) \phi}. \quad (6)$$

The extent or degree of melting F is derived from laboratory experiments or algorithms such as MELTS [Hirschmann *et al.*, 1999] which apply the thermodynamic constraint of minimum free energy based on empirical data. In such experiments, either laboratory or numerical, a selected amount of water is added to a solid of known initial composition and the amount of melt in this closed system is determined. The amount of melt can be expressed as a mole fraction $F(T, p, X_{\text{H}_2\text{O}}, \xi)$ where $X_{\text{H}_2\text{O}}$ is the mole fraction of water in the system, and T is taken from the study of Kelemen *et al.* [2003a]. Relationships of this type derived from MELTS [Hirschmann *et al.*, 1999] are shown

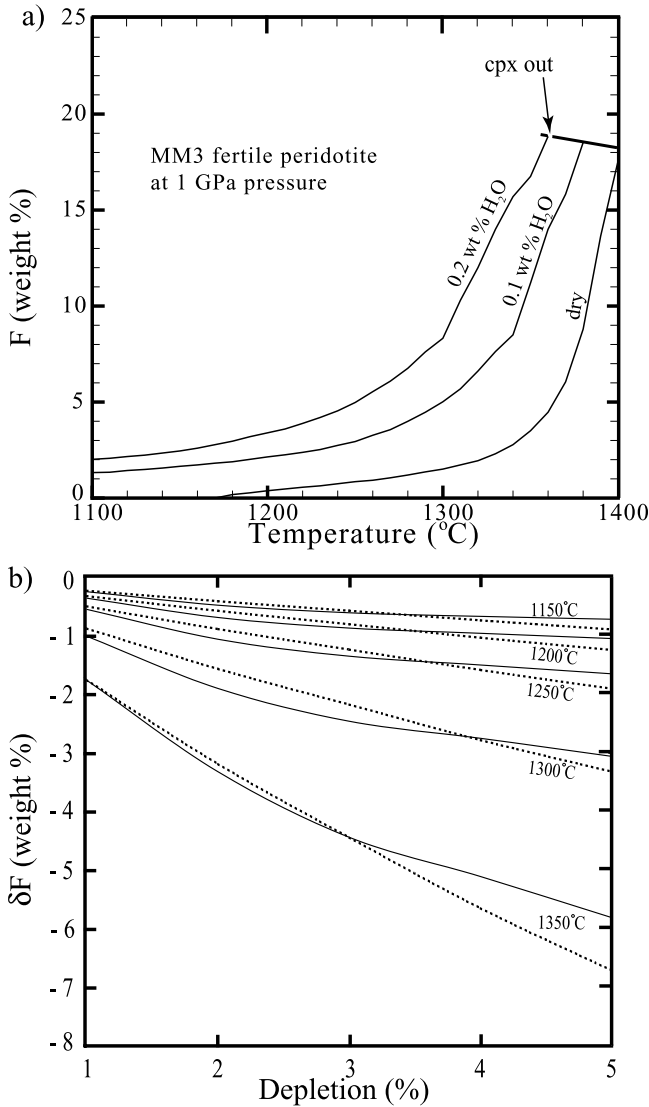


Figure 2. (a) Wet melting of a fertile peridotite composition derived from MELTS [Hirschmann *et al.*, 1999]. The mass fraction of melt in a closed system is shown as a function of temperature for several water mass fractions all at a pressure of 1 GPa. (b) Change in degree of melting (δF) versus depletion for a range of mantle temperatures. Solid lines represent the results from pMELTS [Hirschmann *et al.*, 1999], and the dashed lines represent our approximation to these results ($\delta F/F = 10 \times$ depletion).

in Figure 2a. F is also a function of starting composition of the solid as represented through the variable ξ discussed above. In a more complete treatment like that described above where a range of oxides components is considered, the relative values of N_{SO} for different oxides would be sufficient to describe the depletion of solid by melting.

[16] In treating open system wet melting, we assume equilibrium within each elemental volume so that the composition of the solid and melt instantaneously adjust according to (6). In contrast to the laboratory experiments, X_{H_2O} does not represent the fraction of water initially added

to a closed system but is given in terms of volume fraction of melt and melt composition by

$$X_{H_2O} = \frac{N_{H_2O}\phi}{N_{SO}(1-\phi) + (N_{DO} + N_{H_2O})\phi}. \quad (7)$$

[17] Since we do not distinguish the proportions of individual dissolved oxides in either melt or solid, N_{SO} is appropriately treated as a constant. In models of interest, ϕ is small compared to unity so that

$$F \approx \frac{(N_{DO} + N_{H_2O})}{N_{SO}} \phi \quad (8)$$

and

$$X_{H_2O} \approx \frac{N_{H_2O}}{N_{SO}} \phi. \quad (9)$$

[18] In regions where $F = 0$, we evaluate ϕ by solving (2) with a value of N_{H_2O} for pure water. In such regions, depletion is simply advected with the solid according to (5) with $\Gamma = 0$.

[19] In regions undergoing melting where $F > 0$, ϕ is calculated by rewriting (8) as

$$\phi = \frac{N_{SO}}{N_{DO} + N_{H_2O}} F(T, p, X_{H_2O}, \xi). \quad (10)$$

N_{H_2O} is obtained by solving (2), and N_{DO} is calculated from the identity

$$N_{H_2O}\hat{V}_{H_2O} + N_{DO}\hat{V}_{DO} = 1, \quad (11)$$

where \hat{V}_{H_2O} and \hat{V}_{DO} are the partial molar volumes of water and dissolved oxides, respectively.

[20] Equations (8), (9), and (10) must be satisfied simultaneously. The value of ξ at a given time in (10) is calculated from (5) where for constant N_{SO}

$$\Gamma = N_{SO} \left[\frac{\partial F}{\partial t} + \nabla \cdot (\mathbf{V}_{fluid} F) \right]. \quad (12)$$

The parameterized results of MELTS compiled by Hirschmann *et al.* [1999] were used to model the dependence of the extent of melting (F) on the pressure temperature, and initial water content (X_{H_2O}) (Figure 2a). The parameterization used in this study is simpler than other existing parameterization [Katz *et al.*, 2003] but is sufficient for a first study of the type presented here. The effect of depletion on melting is characterized using the pMELTS program [Hirschmann *et al.*, 1999] in the following way. From an initial MM3 fertile peridotite starting composition, we calculated the residual solid composition after a given amount of melting. Solid of this residual composition was then used as the starting composition to calculate an additional increment of melting of depleted solid. To a reasonable

approximation, the impact of depletion on the extent of melting can be described by the relationship (Figure 2b)

$$\frac{\delta F}{F} = -A\delta\xi, \quad (13)$$

where A is a constant (~ 10). If F exceeds 20%, all of the clinopyroxene is melted out of the unit volume of mantle considered. F is then set equal to 20%, $\delta F = 0$ and in a simple approximation, no further melting occurs. Since the pMELTS program [Hirschmann *et al.*, 1999] is only calibrated to 2 GPa, the effect of pressure on melting at higher pressures is accounted for by prescribing a linear variation of solidus with pressure and appropriately scaling temperatures in Figure 2a with depth. A value of 3°C km^{-1} ($\sim 91^\circ\text{C GPa}^{-1}$) was chosen for the slope of the solidus with depth, derived from the melting temperatures returned from pMELTS [Hirschmann *et al.*, 1999] at 1 GPa and 2 GPa. The latest version of MELTS, pHMELTS [Asimow *et al.*, 2004], is being incorporated in 2-D thermal flow models of subduction zones [Baker *et al.*, 2004]. We used a parameterized version of results from MELTS and pMELTS for simplicity. The thermal models on which the thermal distributions and solid flow are based do not take into account the latent heat of melting or crystallization. If the amount of melting is small ($\sim 5\%$), as is the case in our models, these effects would locally affect temperatures only 100° .

[21] Both hydrous fluid and melt are assumed to migrate by porous flow. When the pressure gradients due to solid flow are sufficiently small, as discussed above, and when the pressure difference between the fluid and solid due to its resistance to compaction is small, the motion of the fluid relative to the viscous solid can be described by the Darcy velocity

$$\mathbf{S} = \frac{\Delta\rho\mathbf{g}k}{\mu_{\text{fluid}}}, \quad (14)$$

where $\Delta\rho\mathbf{g}$ is the pressure gradient that arises from the buoyancy of the fluid and μ_{fluid} is the fluid viscosity. Melt or fluid, with volume fraction ϕ , is assumed to occupy a connected network of fluid-filled pore space in the solid resulting in a permeability, k . The fluid velocity $\mathbf{V}_{\text{fluid}}$ is the sum of the melt velocity relative to the solid, \mathbf{S}/ϕ , and solid flow velocity, $\mathbf{V}_{\text{solid}}$,

$$\mathbf{V}_{\text{fluid}} = \mathbf{V}_{\text{solid}} + \frac{\mathbf{S}}{\phi}, \quad (15)$$

where the solid mantle flow velocity is calculated as in the study of Kelemen *et al.* [2003a].

3. Model Parameters

3.1. Permeability and Fluid Migration

[22] Melts or hydrous fluids with wetting angles smaller than 60° [Mibe *et al.*, 1999] are expected to form a connected network along mineral grain edges [van Barga *et al.*, 1986; Wark and Watson, 1998; Zhu and Hirth, 2003]. This connected grain-scale network yields a grain-

size/melt-fraction-dependent permeability quantified empirically by Wark *et al.* [2003]

$$k = \frac{\phi^3 d^2}{270}, \quad (16)$$

where d is the grain size. Fluid migration along grain edges can be thought of as a minimum scale for melt localization which allows water to interact with the largest possible amount of solid. If melt localized in narrow porous channels by dissolution [Aharonov *et al.*, 1995], by grain size variations in the wedge due to dependence on deviatoric stresses or by anisotropic permeability [Holtzman and Kohlstedt, 2003; Zimmerman *et al.*, 1999], melting could be much more strongly limited by the amount of solid that fluid interacts with. We have restricted the scope of this paper to isotropic and uniform grain sizes to better examine the interplay of temperature, solid flow, water content and depletion on melt production. However, we will comment in the discussion section on how localization could influence the amount of water solid interacts with.

[23] The buoyant migration rate is in part controlled by the density contrast $\Delta\rho$ between rock and fluid and by the fluid viscosity (see equation (14)). In calculating $\Delta\rho$, the fluid was taken to be pure water. This will overestimate the $\Delta\rho$ as silicates combine with water to make melt and thereby decrease $\Delta\rho$. The viscosity of melt with less than 20 wt % water is thought to vary between 1 and 10 Pa s for the depth and temperature range considered in this study [Audéat and Keppeler, 2004]. A constant value of 1 Pa s has been adopted as a first estimate, although the viscosity will vary spatially depending on the composition of the melt. Hydrous fluids coming off the slab may also have a lower viscosity than 1 Pa s [Audéat and Keppeler, 2004] and may therefore have a greater vertical velocity than found in this study. The reduction in density and increase in viscosity would slow the rise of the melt and increase the melt fraction present with respect to the predictions of our models. The effect of these variations on fluid migration in the wedge will be addressed in future studies.

3.2. Water Release From the Slab and Distribution in the Wedge

[24] The water budget of subduction zones strongly depends on the degree of hydration of both the subducting crust and the subducting lithosphere, and may be significantly influenced by regional tectonic settings. The flux of hydrous fluids off the slab may therefore vary considerably between subduction zones. For example, in the Central American subduction zone, the downgoing lithosphere beneath Nicaragua is thought to be heavily faulted and highly serpentinized [von Huene *et al.*, 2000; Rüpke *et al.*, 2002] while the subducting slab beneath Costa Rica is less deeply faulted and consists of thick amphibolitic oceanic crust and oceanic plateau lithosphere [Barckhausen *et al.*, 2001], thereby leading to a larger flux of hydrous fluids off the Nicaraguan slab than the Costa Rican slab [Rüpke *et al.*, 2002]. The models described here assume as a first estimate that water is released along the boundary representing the top of the slab and that the total amount of water released by each crustal column is constant. A total amount of 2.25×10^5 kg of water per m^2 of crustal column was used based on

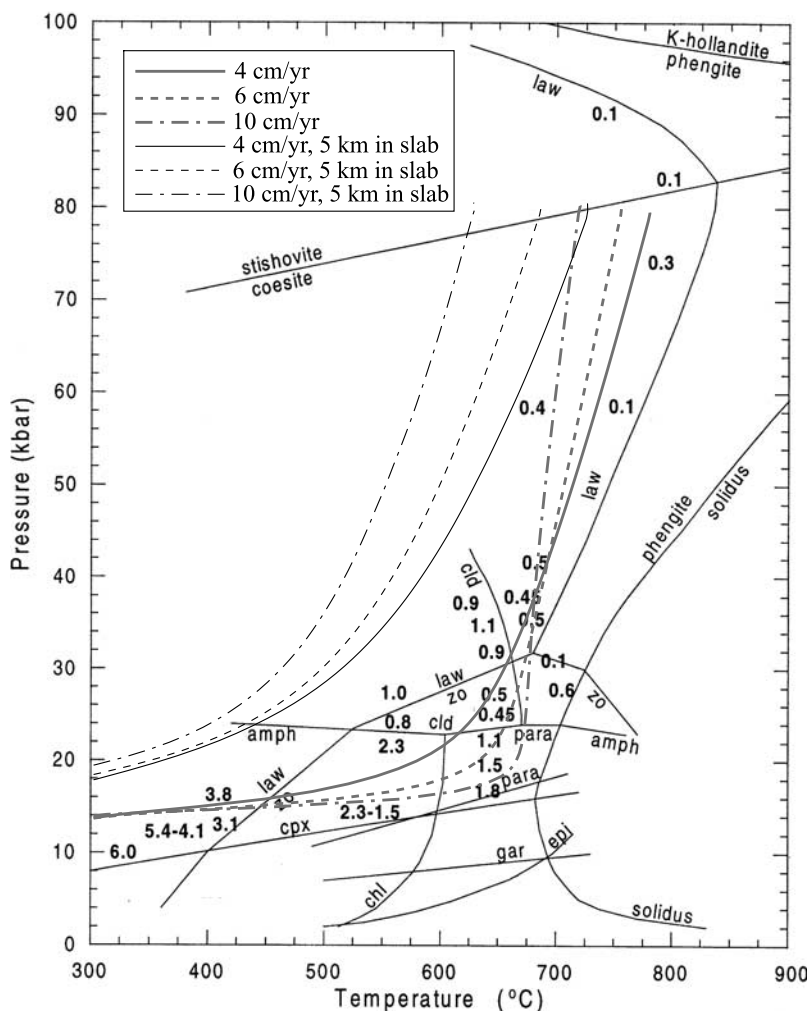


Figure 3. Temperatures along the top of the descending oceanic crust (thick grey lines) and temperatures at the bottom of the 5 km thick crust (thin black lines) for convergence rates of 40, 60, and 100 km Ma^{-1} and a dip of 45° superimposed on a hydrous basalt phase diagram [from *Schmidt and Poli, 1998*]. The wt % of H_2O in the bulk rock bound in hydrous phases for the relevant dehydration reactions are shown in bold. Dehydration reactions occur between depths of 40 and 100 km, though a serpentine or chlorite layer above the slab may redistribute hydrous fluid release (see text). Temperatures along the top of the oceanic crust are higher at higher convergence rate up to 100 km depth. At greater depth, thermal conduction heats the slab top at slower convergence rates, resulting in higher temperatures. A sharp thermal gradient exists between the top and the bottom of the oceanic crust. The cooler temperatures within the oceanic crust may allow for hydrous slab minerals to be stable to great depths.

the estimates of *Schmidt and Poli* [1998]. However, since the overall flux of water off the slab may vary within a given subduction zone, in some cases the flux of water will be varied holding the convergence rate and dip fixed.

[25] The estimates of *Schmidt and Poli* [1998] show that water bound in hydrous phases in the basaltic crust and possibly in serpentinized peridotite in the oceanic lithosphere will be released into the mantle wedge in the depth interval between 80 and 150 km. The depth of specific mineral dehydration reactions within the subducting basaltic crust can be more precisely identified by superimposing temperatures near the slab top from our model on the basalt phase diagram by *Schmidt and Poli* [1998] (Figure 3, thick lines). As the slab top temperatures increase with depth, various hydrous mineral stability fields are crossed and the amount of water bound in mineral phases decreases.

The difference between the amount of water bound in the unstable and stable hydrous minerals is released in the overlying wedge [*Schmidt and Poli, 1998, Table 3*]. For the slab top temperatures for the 40, 60, and 100 km Ma^{-1} convergence rate and 45° dip, the stability fields of lawsonite, zoisite, amphibole, and chloritoid breakdown in the range of ~ 40 to 100 km. Dehydration reactions occur at similar depths for the slab top temperatures for these convergence rates. At shallow depth, slab top temperatures are higher at higher convergence rates but at ~ 100 km depth slab top temperatures for higher convergence rates are lower than for lower convergence rates, thereby reflecting the overall heating of the slab by heat conduction at slower convergence rates. A sharp thermal gradient between the top and bottom of the crust (taken to be 5 km thick, thin lines in Figure 3) is observed for all convergence rates. The base of

the crust remains cooler to deeper depth for higher convergence rates. The stability field of hydrous minerals present in the deep crust therefore extends to greater depths with increasing convergence rates.

[26] As water migrates upward from the slab into the wedge, it may also be bound in hydrous phases in the overlying mantle material, particularly in serpentine and chlorite [Grove *et al.*, 2006]. A cool hydrous mantle layer could therefore develop directly above the slab where temperatures are low enough for serpentine and chlorite to be stable. Such a layer may significantly influence the depth range over which water is released into the wedge. For a convergence rate of 60 km Ma^{-1} , with temperatures shown

in Figure 4a, serpentinization is localized to the subduction “tip” and a thin layer directly above the slab to depths of $\sim 125 \text{ km}$. A chloritized layer with a thickness of roughly 3 km layer also develops just above the slab top down to 130 km depth. Such a layer can hold up to roughly $2.6 \times 10^5 \text{ kg m}^{-3}$ water at depths of 50 to 130 km . Neither serpentine nor chlorite is stable in the wedge above the subducting slab at depths exceeding 130 km . For a convergence rate of 40 km Ma^{-1} , a chloritized layer roughly 4.4 km thick and holding about $3.8 \times 10^5 \text{ kg m}^{-3}$ persists from 50 to 140 km depth. For a convergence rate of 100 km Ma^{-1} , a 2 km thick chloritized layer develops above the slab from 50 to 130 km depth. Such a layer holds $\sim 1.7 \times 10^5 \text{ kg m}^{-3}$ of water. A thin serpentinized layer is also present at convergence rates of 40 and 100 km Ma^{-1} , but its thickness is 600 m or less and would hold at most $6 \times 10^4 \text{ kg m}^{-3}$ of water.

[27] The amount of water that can be bound in the chloritized and serpentinized layer therefore exceeds the amount of water released in the wedge for all three convergence rates. As noted above, the range of depths of water release is significantly redistributed by the progressive thinning of the serpentine and chlorite layer in the mantle above the slab. As a first approach, water released into the wedge by this redistribution is represented by a Gaussian-shaped distribution centered at 115 km depth and with a half width of 40 km that does not change with convergence rate. Furthermore, the development of a hydrated and buoyant serpentinized or chloritized layer directly above the slab may result in the generation of Rayleigh-Taylor instabilities and the vertical migration of diapirs into the wedge which are colder than the surrounding mantle [Gerya and Yuen, 2003]. To keep these first models simple, such a process is not explicitly taken into account.

4. Numerical Method

[28] Finite difference approximations of equations (2), (5), (8), (9), and (10) are solved numerically. In equations (2)

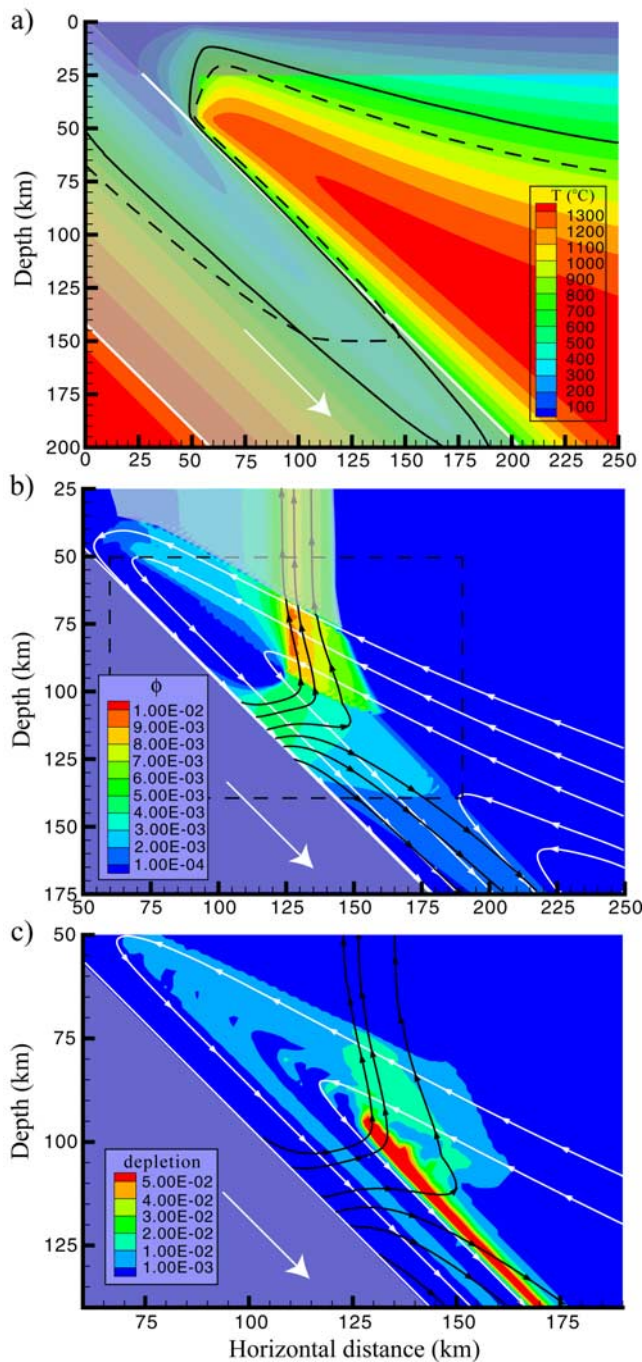


Figure 4. (a) Temperature distributions for a convergence rate of 60 km Ma^{-1} , a slab age of 90 Ma , and a dip of 45° . Serpentine and chlorite stability fields, derived from phase diagrams from Schmidt and Poli [1998] are superimposed (solid and dashed, respectively). The serpentine and chlorite layers redistribute the water released by slab dehydration reactions into a broad dehydration pulse (see text). (b) Fluid distribution. Fluid is released from the slab at a rate based on the results of Schmidt and Poli [1998] and follows a Gaussian distribution centered at a depth of 115 km with a half width of 40 km . Fluid rises by buoyant porous flow along grain edge channels with a permeability based on a uniform grain size of 1 mm . Melting occurs where hydrous fluids interact with hot mantle. Solid flow (shown by white streamlines) in the mantle wedge generated by the motion of the plate is calculated according to a temperature-dependent viscosity based on thermally activated creep (see text). Fluid flow lines are shown in black. (c) Mantle depletion. Values reflect the amount of melt extracted from the solid mantle or F . Fluid flow lines are shown in black, and solid flow lines are shown in white.

and (5), advection terms are approximated with a finite upwind method corrected for numerical diffusion [Smolakiewicz, 1983] and a forward time difference. Depletion in the wedge is tracked with a tracer algorithm, where tracers are assigned the average value of depletion at a cell and then advected by the solid mantle flow [cf. Tackley and King, 2003]. This gives an explicit time stepping procedure, where a Courant criterion is used to limit the time step size. In principal, values derived at each time step of (2) and (5) should simultaneously satisfy (8), (9), and (10). In practice, these relationships are satisfied only at the beginning of each time step. An alternative, slightly more accurate approach would be to satisfy relationships (8), (9), and (10) both at the beginning and at the end of the time step, but then the solution for each time step becomes iterative. In this first study we have employed the simpler fully explicit procedure restricting the time step to be small enough to ensure accuracy.

5. Dimensionless Scaling

[29] A number of physical parameters influence fluid migration. These include density difference between melt and solid, fluid viscosity, grain size, and the rate of water release. Dimensionless parameters are therefore valuable in assessing the relative effects of these different physical parameters. For fluid migration above a subducting plate, the ratio of fluid velocity to solid velocity controls the amount by which fluid flow will be deflected by the solid flow. Using expressions for Darcy velocity (14) and permeability (16) and denoting the volume fraction of water where it is released at the slab top as ϕ_0 , the ratio of liquid to solid velocity scales as

$$\frac{\Delta\rho g k}{\phi_0 \mu_{\text{liquid}} u_{\text{slab}}} \propto \frac{\Delta\rho g \phi_0^2 d^2}{\mu_{\text{liquid}} u_{\text{slab}}}. \quad (17)$$

The value ϕ_0 may be expressed in terms of the rate of water release, W , as

$$W = \frac{\Delta\rho g}{\mu_{\text{liq}}} k \propto \frac{\Delta\rho g}{\mu_{\text{liq}}} \phi_0^3 d^2. \quad (18)$$

Solving for ϕ_0 and substituting in equation (17) gives the ratio of liquid to solid velocity as

$$\frac{W^{2/3}}{u_{\text{slab}}} \left(\frac{\Delta\rho g d^2}{\mu_{\text{liq}}} \right)^{1/3}. \quad (19)$$

Fluid flow lines below the melting region remain unaffected by any change in physical parameters that leaves this single dimensionless parameter unaltered. The fraction of water carried to greater depth is only a function of the flow line geometry and should increase as the ratio of fluid velocity to solid velocity decreases. With W approximately proportional to u_{slab} , u_{slab} must be varied in proportion to d^2 to maintain constant flow line geometry. Lowering fluid viscosity while holding other parameters fixed would increase fluid velocity and limit the effect of solid flow on fluid distribution. Since melting enhances the amount of fluid present, this scaling

applies only to the water distribution below regions where melting occurs.

6. Results

[30] To investigate the impact of solid flow on fluid migration and melt production, we varied (1) the convergence rate from 40 to 100 km Ma⁻¹ holding the slab dip and grain size constant; (2) the distribution of water released by dehydration holding grain size, convergence rate and slab dip constant; (3) the mantle temperature from 1350°C to 1380°C holding convergence rate, slab dip and grain size constant; (4) the grain size from 0.3 to 3 mm holding convergence rate and slab dip constant; and (5) the slab dip from 30° to 60° holding convergence rate and grain size constant. Parameters that may be important but which were not varied include the location and rate of back-arc spreading, the likely effects of hydration on mantle rheology [Cagnioncle and Parmentier, 2006; Arcay et al., 2005; Gerya and Yuen, 2003], and the age of the subducting plate.

6.1. Effect of Solid Mantle Flow

[31] Solid mantle flow greatly influences wet melting in the wedge. First, solid flow influences the trajectories of hydrous fluids released by the slab, thus controlling the fraction of fluid released that rises into the hot center of the wedge. Second, solid flow supplies fertile mantle to the wet melting region and removes mantle depleted by melting. Continuous melting cannot occur within a static solid matrix because the solid would become increasingly depleted until further melting is impossible. Finally, temperatures in the wedge and along the slab top increase with increasing convergence rates: The enhanced wedge flow due to increased convergence rates, combined with the temperature-dependent viscosity, brings hotter mantle from deeper depths further into the wedge corner, thereby broadening the region over which wet melting can occur.

[32] These effects of solid flow are illustrated in Figure 4 for a uniform grain size of 1 mm and a convergence rate of 60 km Ma⁻¹. Water rises buoyantly from the slab as discussed above (Figure 4b). Part of this water is advected downward to greater depth by the solid flow as described by the ratio of fluid velocity to solid velocity (equation (19)) and will potentially be incorporated into transition zone mineral phases. This water will not contribute to wet melting, thus limiting the amount of melt that can be generated. The remainder of the water rises buoyantly into regions that are hot enough and where the pressure is low enough for wet melting to occur. The greatest amount of melting occurs across a narrow front where fluid rising from the slab first encounters mantle that is hot enough to melt. This can be seen in Figure 4c as melting reactions deplete the solid mantle. Above this region lower extents of melting continue as water rich melt interacts with mantle material at lower pressures.

[33] Melt at the top of the melting region would freeze as it moves toward lower temperatures if it were not extracted. However, our models implicitly assume that all melt is extracted at the top of the melting region. If this were not so, a crystallization region would develop in solid flowing into the wedge, as freezing of melt enriches that mantle in melting components. This enriched mantle would eventually

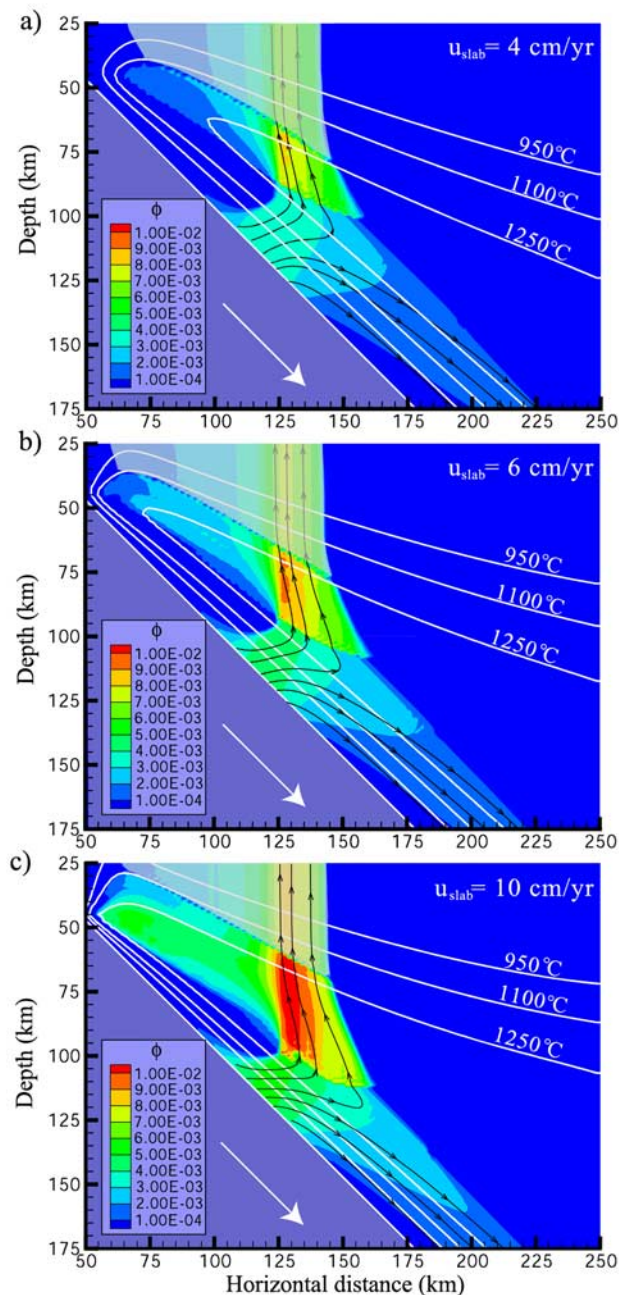


Figure 5. Fluid volume fraction in the mantle wedge for (a) 40, (b) 60, and (c) 100 km Ma^{-1} . Other parameters are as in Figure 4. Melt flow lines are shown in black, and temperature contours for 950°C, 1100°C, and 1250°C are shown as white lines. If melt were to be extracted by vertical transport through the cold lithosphere, the width of the region of melt distribution in the wedge would give an indication of the range of volcano positions. Higher convergence rates carry melt closer to the convergent boundary. However, as the convergence rate increases, both the back-arc boundary of the wet melting region and the region of highest degree of melting remain relatively fixed.

flow through the wedge and be entrained in the downward flow along the top of the slab (Figure 4c). This would be the first solid with which water rising from the slab interacts. The masked fluid distribution above the melting region seen in Figure 4 is due to the upward percolation of the water that remains after freezing of the melt and has no bearing on melt distribution. This would not be expected to occur with more realistic models of melt extraction through the lithosphere. Quantitatively predicting the surface distribution of volcanism is beyond the scope of these models, but we will comment on it in the discussion.

6.2. Influence of Convergence Rate

[34] These effects of solid flow on melt production can be illustrated by varying the convergence rate. As shown in Figure 5, lower convergence rates, such as 40 km Ma^{-1} (Figure 5a), yield less melt present and a weaker extent of melting compared to 60 km Ma^{-1} , while higher convergence rates, such as 100 km Ma^{-1} (Figure 5c), yield a greater amount of melt present and a greater extent of melting. This melting trend is reflected in the melt production rate (for a grain size of 1 mm) which correspondingly increases with convergence rate (Figure 6a). If the fraction of fluid rising into the hot region of the wedge and the wedge temperatures were held fixed, the melt production should be simply proportional to the convergence rate, with a trend illustrated by the dotted line in Figure 6a. Two opposing effects influence melt production rates with increasing convergence rate: the overall increase in temperatures encountered by fluids (in contrast to the potential temperature which remains fixed at 1350°C unless otherwise specified) and the reduction in the flux of water supplied to the melting region. The temperature encountered by fluids in the region of greatest melting increases by 70°C from 40 to 100 km Ma^{-1} . For convergence rates ranging from 40 to 100 km Ma^{-1} , the fraction of the water released by dehydration that gets entrained to greater depth by solid mantle flow rises from 32.7% to 51%. The two melt production trends present in Figure 6a for a 1 mm grain size indicate that the effect of the reduced fraction of water rising into the wedge has a larger influence than the effect of increasing temperature along the melting front: Melt production first increases roughly linearly proportional to convergence rate but at higher convergence rates, melt production increases more slowly. Melt production is thus limited by the amount of water supplied to the melting region since the increase in solid mantle flow above the slab with increasing convergence rates carries a greater fraction of water to depth.

6.3. Influence of Buoyant Melt Migration Rate

[35] Grain size, $\Delta\rho$ and μ_{fluid} affect fluid velocity through the permeability relationship (see equation (16)) and is therefore an important factor in determining the flux of water that rises into the melting region. However, buoyant melt migration rate is controlled the combination of the physical parameters $\Delta\rho d^2/\mu_{\text{fluid}}$. Increasing grain size in the wedge is thus equivalent to decreasing fluid viscosity or increasing $\Delta\rho$. For example, increasing the grain size by a factor of 3 is equivalent to decreasing μ_{fluid} by roughly an order of magnitude. In the following section we will discuss the effect of changing melt transport rate as a consequence

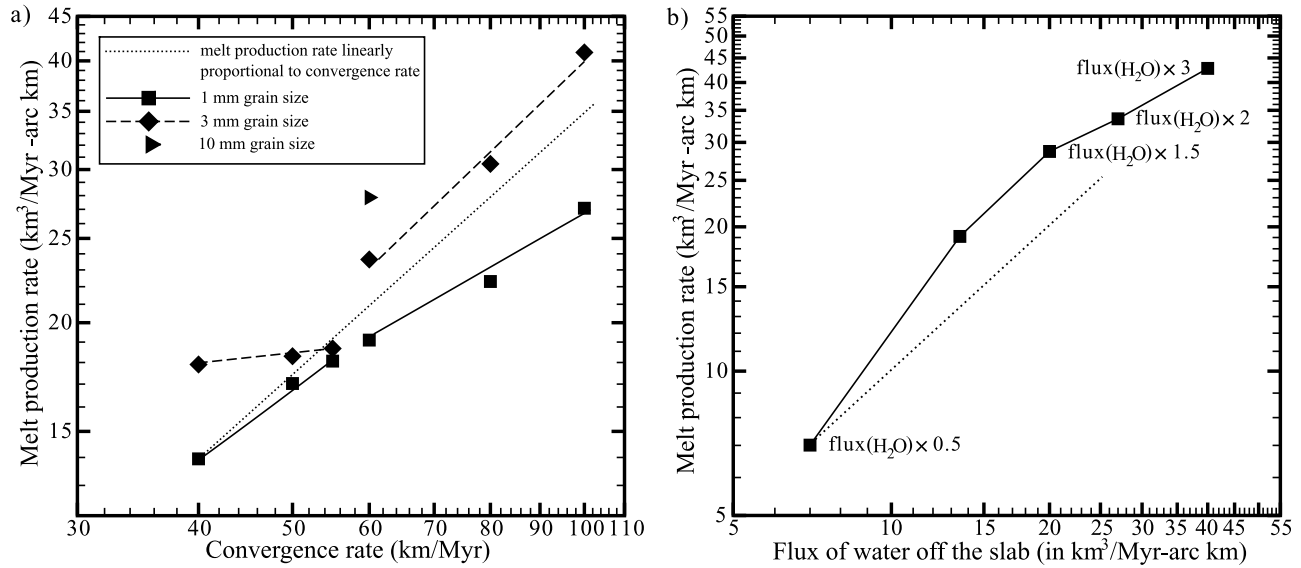


Figure 6. (a) Log-log plot of the melt production rate (in $\text{km}^3 \text{Ma}^{-1} (\text{arc km})^{-1}$) versus convergence rate (in km Ma^{-1}) for the cases shown in Figures 4 and 5. Squares with a solid line represent the results from our models with a uniform grain size of 1 mm, diamonds with a dash-dotted line represent the results for a uniform grain size of 3 mm, and the dotted line represents the results for melt production rates increasing linearly with convergence rates. The right triangle corresponds to a convergence rate of 60 km Ma^{-1} and a 10 mm grain size. Pressure increases along the melting front with increasing convergence rate, while the fraction of water reaching the melting region decreases for a fixed 1 mm grain size. These effects prevent the melt production rate to increase proportionally with convergence rate. At larger grain sizes, fluids are not as strongly influenced by solid flow, and a larger fraction of fluids reaches the melting region. Melt production rates are consequently proportional to convergence rates at high convergence rates. (b) Log-log plot of the melt production rate (in $\text{km}^3 \text{Ma}^{-1} (\text{arc km})^{-1}$) versus flux of water off the slab (in $\text{km}^3 \text{Ma}^{-1} (\text{arc km})^{-1}$) for a convergence rate of 60 km Ma^{-1} and slab dip of 45° . The dotted line corresponds to melt production rates increasing linearly with increasing flux of water off the slab.

of varying grain size, but the equivalent variations in fluid viscosity and density differences should be kept in mind.

[36] Figure 7 shows the result of varying grain size by an order of magnitude for a fixed convergence rate of 60 km Ma^{-1} and a slab dip of 45° . For small grain sizes (0.3 mm), all the water released by mineral dehydration is carried to greater depth by solid flow so that it does not rise and cause melting in the hot wedge (Figure 7a). With 1 and 3 mm grain sizes (Figures 7b and 7c), water rises into the wedge and melting occurs. For the 3 mm grain size, less melt is present in the melting region due to the high flux of melt in this region, but the overall extent of melting is greater. Melt production rates for grain sizes of 1 and 3 mm are $18.2 \text{ km}^3 \text{Ma}^{-1} \text{ km}^{-1}$ and $23.4 \text{ km}^3 \text{Ma}^{-1} \text{ km}^{-1}$, respectively. In the 3 mm case the width of the region through which water rises is very similar to that in the 1 mm case, but for the 3 mm case the flux of water through this region is greater as shown by fluid flow lines in Figures 7b and 7c.

[37] The dependence of melt production rate on convergence rate is reversed for the 1 and 3 mm cases. In the 1 mm case discussed above the melt production depends overall more on the fraction of water rising to the melting front, while in the 3 mm case, melt production is influenced more strongly by temperatures along the melting front. Indeed, compared to the 1 mm case the flux of water through the melting region is significantly larger and varies less between convergence rates: For $d = 1 \text{ mm}$, the fraction of water

which rises to the melting front varies from 67.3% at 40 km Ma^{-1} to 49% at 100 km Ma^{-1} , while for $d = 3 \text{ mm}$, it varies from 89.6% to 82.9%. Therefore, at larger grain sizes, higher temperature mantle material is exposed to significantly higher water contents as convergence rate increases. At lower water content, the melting curve in Figure 2a is relatively flat with increasing temperature. This translates in a smoother increase in melt production rates with increasing convergence rate, as observed for the 1 mm case. However, at higher water content, the melting curve increases more rapidly with temperature, which in turns lead to a change in melt production regime from being weakly dependent on convergence rate for convergence rates below 60 km Ma^{-1} to nearly linearly proportional to convergence rate above 60 km Ma^{-1} .

[38] Recrystallization piezometers for olivine suggest that the average grain size of a deforming rock evolves toward a value which varies inversely with deviatoric stress σ : $d = d_0 \sigma^{-r}$, where d_0 and $r \approx 1$ are empirically determined constants (van der Waal *et al.* [1993] and Hirth and Kohlstedt [2003] found $r \sim 1.3$). In a dislocation creep regime, $\dot{\epsilon} \propto \sigma^3$, so the grain size is approximately inversely proportional to the third power of strain rate. The strain rate may be scaled as $\dot{\epsilon} = u_{\text{slab}}/L$, where L corresponds to the average depth of slab mineral dehydration. Neglecting local areas of increased deformation, we therefore expect that the grain size in the wedge should vary as $d \propto u_{\text{slab}}^{-1/3}$. The grain

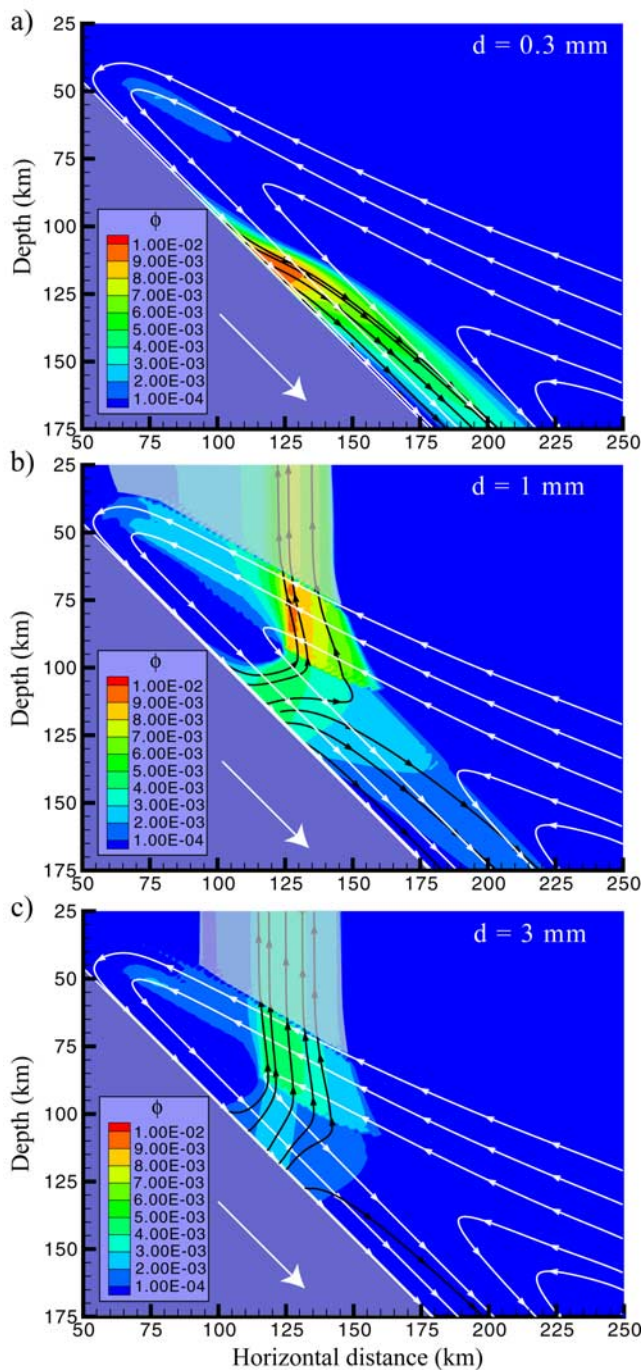


Figure 7. Fluid volume fraction in the mantle wedge for a convergence rate of 60 km Ma^{-1} and grain sizes of (a) 0.3 mm , (b) 1 mm , and (c) 3 mm . Fluid and solid flow streamlines are shown in black and white, respectively. Wet decompression melting is observed in all three cases. For small grain sizes, however, low permeability restricts the buoyant rise from fluids off the top of the slab so that the fluid is carried downward into the mantle.

size for the convergence rate of 60 km Ma^{-1} is fixed through out the wedge at 1 mm and the grain sizes for the other convergence rates are prescribed accordingly. The results do not qualitatively differ from those for a uniform grain size of 1 mm shown in Figures 4 and 5. For a 100 km

Ma^{-1} convergence rate, the smaller grain size ($d = 0.86 \text{ mm}$) hinders the buoyant rise of the water released from the slab. Solid flow above the top of the slab therefore carries a larger portion of the water down to greater depth (about 54.7%), thereby limiting the amount of wet melting in the wedge. The melt present is advected toward the wedge corner by solid flow, yielding a wider region of volcanism and a volcanic front that is close to the convergent boundary. The lowest convergence rates has the largest grain size ($d = 1.17 \text{ mm}$). Fluid therefore rises more rapidly and only 16% of the water is advected to greater depths. The remaining water can efficiently percolate into the hot mantle and provoke melting. The higher melt velocities limit the influence of solid mantle flow on melt distribution in the wedge and yield a narrow region of possible arc volcanism. However, larger grain sizes, and therefore increased fluxes of water through the melting region, do not necessarily correspond to larger melt production rates. Indeed, increased water fluxes focus water into a narrower melting region, thereby leading to high values of depletion and lower values in melt production rate increase. At smaller grain sizes (such as 1 mm) water is distributed by solid flow and a wider, more fertile, melting region is sampled, which can potentially yield larger melt production rates.

6.4. Influence of the Flux of Water off the Slab

[39] As mentioned in the model parameter section, the flux of water off the slab may vary considerably within a single subduction zone. In order to investigate the influence of the flux of water off the slab on melt production, the convergence rate (and therefore the temperature distribution) and grain size were held fixed at 60 km Ma^{-1} and 1 mm , respectively. The flux of water off the slab was then either decreased by half or increased up to 3 times its standard value of $13.5 \text{ km}^3 \text{ Ma}^{-1} (\text{arc km})^{-1}$ used previously. The melt production rates obtained for these different fluxes of water are shown in Figure 6b. Two melt production trends emerge. At low water flux, the rate of melt production is more than linearly proportional to the flux of water off the slab because an increasing fraction of the released water reaches high-temperature regions of the wedge. At higher fluxes, solid flow appears limit the amount of fertile mantle advected into the melting region thus limiting melt production rates. In this case, melt production increases less than linearly proportional to the flux of water off the slab. Melt production rates therefore do not simply increase linearly with increasing flux of water off the slab: The rate at which solid flow brings fertile mantle material into the melting region limits the amount of melt produced with increasing water fraction.

6.5. Influence of Thermal Structure

[40] A mantle potential temperature of 1350°C was assumed for all of the cases discussed thus far. In order to explore the importance of thermal structure on melting at convergent plate boundaries, we increased this temperature to 1380°C for a convergence rate of 60 km Ma^{-1} and slab dip of 45° . Fluids were released from the top of the slab over the same depths range as before and the grain size through out the wedge was 1 mm . Such a small change in potential temperature does not noticeably alter solid flow in the wedge. Changes in melting behavior are hence exclu-

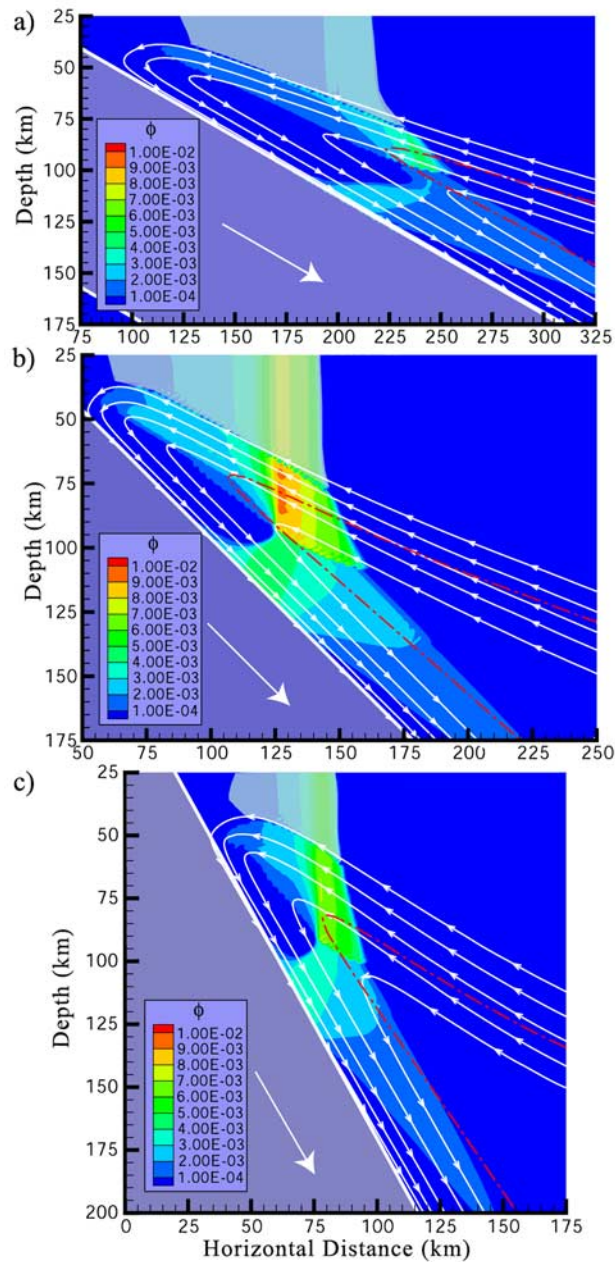


Figure 8. Fluid volume fraction in the mantle wedge for a convergence rate of 60 km Ma^{-1} and a slab dip varying between (a) 30° , (b) 45° , and (c) 60° . Solid flow lines are shown in white. The 1300°C isotherm is shown as a dash-dotted red line. The same flux of water is released over the same depth range for all dips. The fraction of water advected to greater depth by solid flow increases with decreasing dip.

sively due to the increase in temperature in the wedge above the subducting slab. The 30°C increase in mantle potential temperature yields a melt production rate of $25.2 \text{ km}^3 \text{ Ma}^{-1} (\text{arc km})^{-1}$. This melt production rate increase is larger than that resulting from enhancing the flux of water through the melting region by increasing grain size from 1 to 3 mm but less than from 1 to 10 mm (Figure 6a) and is almost

equivalent to increasing the flux of water off the slab by 50% (Figure 6b). Mantle potential temperatures beneath back-arc spreading centers can vary from $\sim 1350^\circ\text{C}$ (East Scotia ridge, Mariana trough) to $\sim 1500^\circ\text{C}$ (Manus Basin [see Kelley *et al.*, 2006, Figure 2]). Mantle potential temperatures in the wedge similar to those found at back-arc spreading centers could be reflected in significant variations in melt production rates between subduction zones. Furthermore, the melting relationship for mantle flowing into the wedge depends on initial mantle composition. Models with higher mantle potential temperature may hence act as surrogates for mantle compositions with lower melting temperature.

6.6. Influence of Slab Dip

[41] Slab dip influences both the thermal structure and solid velocity distribution. For fixed slab velocity, thermal boundary layers at the top of the wedge and the top of the slab remain approximately constant in thickness. Therefore, although the maximum temperature remains almost the same for the range of slab dips, the depth interval outside the thermal boundary layers increases with increasing dip as can be seen through the increasing height of the greater than 1300°C region with increasing dip in Figure 8. However, this larger high-temperature region with increasing dip do not yield higher melt production rates: The melt production rates for a given flux of water released over the same depth range vary from 2.5 to $18.2 \text{ km}^3 \text{ Ma}^{-1} (\text{arc km})^{-1}$ between 30° and 45° and decrease to $10.4 \text{ km}^3 \text{ Ma}^{-1} (\text{arc km})^{-1}$ for a dip of 60° .

[42] This decrease in melt production is due to the influence of solid velocity on the path of water through the wedge. Indeed, at a given convergence rate (60 km Ma^{-1} here), the magnitude of velocities in the wedge is almost independent of dip. At shallow dips, the horizontal component of solid flow dominates over the vertical component. Since fluids are released over a wider horizontal extent, the overall flux of water off the slab, and hence fluid velocity, is decreased with respect to a 45° dip. The horizontal component of solid flow is hence larger than the fluid velocity and carries most of the initially released water to greater depth (80.6%). The remaining hydrous fluid, combined with overall low wedge temperatures, induce little melting which, in turn, is advected close to the convergent boundary by the horizontal component of solid flow (Figure 8a). For a 60° dip, water is released over a smaller region, thereby yielding larger fluid velocities than for a 45° dip. A smaller fraction of water therefore gets carried down to greater depth by the vertical component of solid flow than at a 45° dip (19.4% versus 41%). The remaining water crosses the 1300°C isotherm over a smaller region than in the 45° dip case, thereby yielding smaller melt production rates. Such a decrease would not be observed if water were released at greater depths for larger dips, leading the hydrous fluids to encounter hotter mantle material and to thereby generate more melt.

7. Discussion

[43] Important feedbacks between temperature distribution, solid flow and wedge rheology were described in the results section. We found that increasing convergence rates

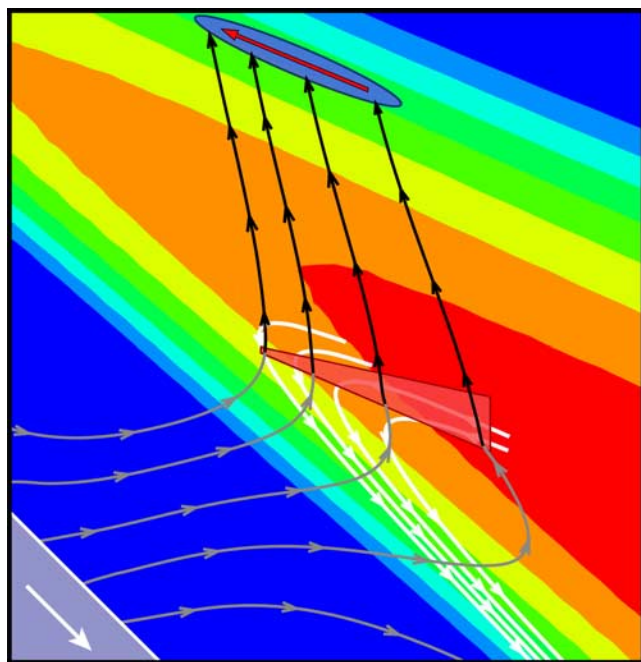


Figure 9. Schematic diagram of fluid migration at subduction zones. Hydrous fluids (grey streamlines) are released from the slab by dehydration reactions and rise buoyantly into the wedge. Fluids do not rise vertically into the wedge but are influenced by solid flow. A melting front (pale red triangle) develops where the water which was not advected to greater depth reaches a region hot enough to melt. The fluid is then a mixture of dissolved oxides and a hydrous component (black streamlines). The large fluid fraction after melting front prevents solid flow from affecting fluid migration, and fluids migrate vertically to the surface until they reach colder temperatures (pale blue ellipse). The present study does not explicitly treat the final fate of melt, but a potential melt transport mechanism, shown by the red arrow, is discussed in the text.

at a fixed dip and constant amount of water released has two opposing effects on melt production: It simultaneously broadens the potential melting region, which increases melt production rates but reduces the flux of water to that melting region by advecting a greater fraction of released water to greater depth. This latter effect can be offset to a certain extent by increasing grain sizes which increases fluid velocities: Increasing the grain size by a factor of 3 increases the permeability by a factor of 9 (equation (16)). The influence of solid flow on fluid migration is thereby diminished and the flux of water through the melting region enhanced.

[44] Melt production rates do not simply increase linearly with increasing flux of water off the slab at a fixed convergence rate and grain size but are rather influenced by the rate at which solid flow brings fertile material to the wet melting region. Increasing dip angle while holding convergence rate fixed both increases the overall wedge temperature and varies the influence of solid flow on the fluid distribution.

[45] Seismic, geochemical, and petrological studies provide valuable constraints on the physical processes occur-

ring at subduction zones. The simplicity of our models, which consider no oblique convergence, a constant incoming plate age, and steady state temperature distributions and solid and fluid velocities, contrasts with the complexity of many convergent boundaries. However, comparisons between simplified models and actual subduction zones may allow a better delineation of the physical factors that influence arc magmatism.

7.1. Melt Production With Increasing Convergence Rate and Varying Dip

[46] Figure 9 is a schematic representation of wet melting in the wedge and its relationship to temperature, fluids/melt and solid flow distributions. Hydrous fluids released by dehydration reactions (grey streamlines) are deflected by solid flow and thus in general do not rise vertically through the wedge. As previously noted, a fraction of the released water will be advected down to greater depth by solid flow. The remaining water rises buoyantly in the wedge until it encounters mantle with a temperature above the wet solidus. The resulting melting front (pale red triangle), which represents a relatively thin region where most melt is produced, is oblique to isotherms, with temperatures along the melting front increasing with increasing pressure along a wet solidus. Within the melting region, melt production is limited both by the rate at which solid flow (white streamlines) brings fertile solid material into the region and the rate at which hydrous fluids rise upward through the melting front.

[47] In the region above the melting front, melt which flows along the black streamlines in Figure 9 is composed of both dissolved oxides and hydrous fluid. Though melt may still be moving toward lower pressure and higher temperature into mantle that has been only slightly depleted by previous melting, melt production is limited by the increasing saturation of silicate melt with hydrous fluid (or the saturation of hydrous fluid with dissolved oxides). Consequently, melt moving through this region provokes only a small additional extent of melting (see Figure 4c). The total height over which the wet solidus is exceeded in the wedge, what some would inappropriately term the “melting column,” therefore exerts a secondary effect on melt production. As melt migrates to the surface, it encounters temperatures below the solidus (pale blue region in Figure 9). The present study does not explicitly treat the final fate of melt, but one possibility is discussed later.

[48] The pressure range over which most of the melting occurs along with the extent of melting (F) is shown as a function of convergence rate in Figure 10. The range of pressures at which melting occurs increases by ~ 0.85 GPa (or ~ 25 km) as convergence rate increases from 40 to 100 km Ma^{-1} . The pressure of melting is controlled by the trajectories of fluid off the slab. Mantle material hot enough to melt is present closer to the slab with increasing convergence rate. The pressure of melting consequently increases with increasing convergence rates. However, the extent of melting increases with increasing convergence rate, indicating that the effect of increasing temperature has a stronger effect than pressure. The amount of water fluxed through the melting region also has a significant influence on F : The extent of melting is systematically larger for more rapid melt transport (grain size of 3 versus than 1 mm) due to the

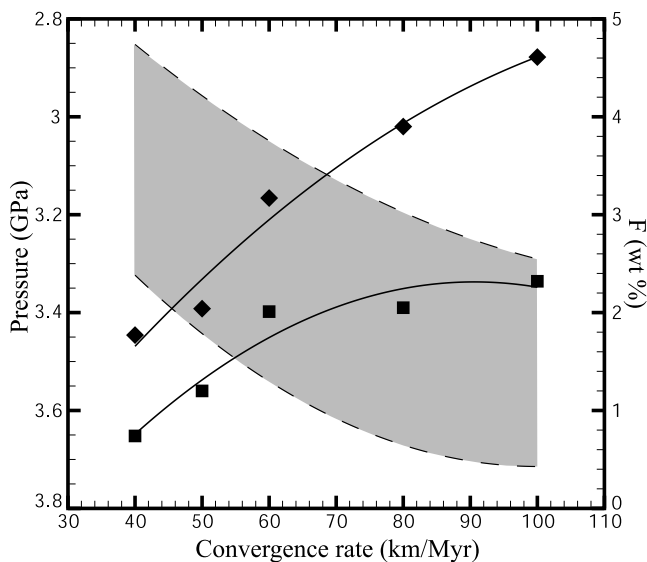


Figure 10. Pressure of melting (in GPa) and extent of melting (F in wt %) as a function of convergence rate. The range in pressure (shaded region between the dashed lines) corresponds to the range in depth of the melting front for a given convergence rate. Squares and diamonds correspond to F for grain sizes of 1 and 3 mm, respectively. F increases with increasing convergence rate even though the pressure of melting also increases. The maximum temperature along the melting front, which also increases with increasing convergence rate, has therefore a larger influence on F than pressure. F increases with increasing grain size due to the larger fraction of water reaching the melting region.

larger amount of water reaching the melting front. This increased water fraction, combined with temperatures along the melting front that increase with convergence rate, result in a significant increase in F with both grain size and convergence rate.

[49] With increasing slab dip at a fixed grain size of 1 mm, F first increases by ~ 2 wt % from 30° to 45° and then decreases by ~ 1 wt % from 45° to 60° . The distribution of F for a grain size of 3 mm mirrors the one described for 1 mm. Similarly, the pressure at which melting occurs first increases by ~ 0.44 GPa (or ~ 13 km) as the slab dip is increased from 30° to 45° and then decreases by roughly the same amount as slab dip increases from 45° to 60° . These behaviors can be understood in light of the influence of solid flow on fluid trajectories and of the position of isotherms above the wet solidus (represented in Figure 8 by the 1300°C isotherm) with respect to the fluid trajectories. As explained above, fluids are less deflected by solid flow at larger slab dips, thereby increasing the fraction of water reaching the melting front and decreasing the pressure range of that melting front. The position of isotherms above the wet solidus determines the potential melting pressure range. For a 45° dip, all of the hydrous fluids reach a region with temperatures above 1300°C (Figure 8b), yielding a high average temperature along the melting front and allowing for a wide range of melting pressures and a large F . On the other hand, for a slab dip of 60° , a large fraction of hydrous fluids do not cross the 1300°C

isotherm (Figure 8c), yielding a lower average temperature along the melting front. Lower F values (~ 1 wt %) and a smaller range of melting pressures are consequently found. Increasing the grain size from 1 mm to 3 mm diminishes the influence of solid flow on fluid migration. A larger fraction of water reaches the melting region and a larger F is observed.

7.2. Comparison With Aleutian Arc Magma Chemistry

[50] The relatively simple geometry of the Aleutian subduction zone westward of the continental shelf (particularly the absence of a back-arc basins, the lack of a thick overriding continental lithosphere, a relatively uniform slab age and an arc-normal convergence rate that varies uniformly along the arc) provides a unique setting to begin the comparison between our models and an oceanic-oceanic subduction zone. Chemical variations in Aleutians magmas have been attributed to a source composition that is a variable mixture of subducted oceanic crustal and sedimentary components with a depleted mid-oceanic ridge-type mantle [Kay and Kay, 1994, and references therein]; to an upper mantle source composed of different proportions of mid-oceanic ridge and oceanic island-type components [Morris and Hart, 1983]; or to the relative age of the magmatic centers which influences the amount of wall rock contamination of the magma during its ascent through the lithosphere [e.g., Myers et al., 1985]. Most of these previous explanations, however, were based solely on geochemical and petrological inferences. Prediction of our simple models over the parameter space explored in this study allows us to assess the possible importance of physical processes influencing the extensive geochemical and petrological data available [e.g., Kelemen et al., 2003b, and references therein].

[51] Geochemical indicators such as MgO, SiO₂, and K₂O concentrations in primitive melts (Mg# $\geq 60\%$) yield insight into melting processes (based on the compilation of Kelemen et al. [2003b, and references therein]) (Figure 11). The orthogonal component of convergence rate with respect to the convergent boundary, or “updip” convergence rate, decreases from east to west along strike in the Aleutians. The updip convergence rate decreases from ~ 60 to 75 km Ma⁻¹ in the eastern Aleutians to less than 40 km Ma⁻¹ in the western Aleutians. Slab dip increases from $\sim 45^\circ$ in the eastern Aleutians to $\sim 60^\circ$ in the west. Such a variation in updip subduction rate and slab dip with other parameters relatively fixed within a subduction zone provides a unique setting to apply the understanding of wet melt production processes gathered from our models.

[52] MgO concentrations yield primitive magma temperatures estimates based on equilibrium Mg partitioning between olivine and melt [Gaetani and Grove, 1998]. A systematic, along-strike decrease in MgO concentration with decreasing convergence rate (increasing longitude) is observed (Figure 11a), reflecting an overall decrease in primitive magma temperatures with decreasing convergence rate from $\sim 1350^\circ$ to $\sim 1200^\circ\text{C}$ [Kelemen et al., 2003b]. This decrease in temperature is consistent with our models in which the overall temperatures along the melting front decrease with decreasing convergence rate (Figure 5) even though the mantle potential temperature is held fixed at 1350°C . Considerable variations in wedge mantle potential

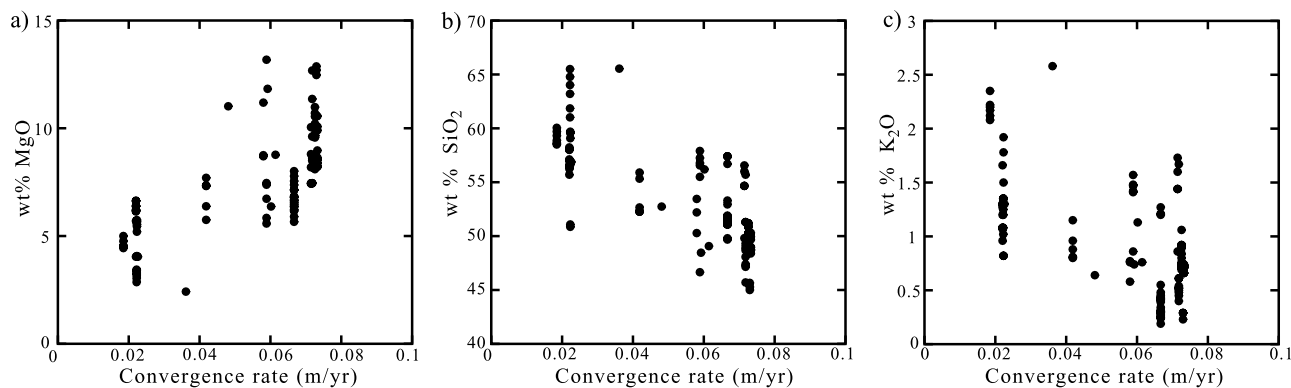


Figure 11. Variation of (a) MgO, (b) SiO₂, and (c) K₂O concentrations for primitive magmas (Mg# > 60%) with a convergence rate along the Aleutian arc [Kelemen *et al.*, 2003b]. MgO concentrations increase with increasing convergence rate (increasing longitude), indicating that the primary magma temperatures in the western Aleutians are lower than in the eastern Aleutians. The decrease in SiO₂ concentrations with increasing convergence rate corresponds to an increase in melt/mantle equilibration pressure. The increase in K₂O concentrations to the west suggest a smaller extent of mantle melting in the western Aleutians than in the eastern Aleutians.

temperatures, such as those inferred in back arcs [Wiens *et al.*, 2006; Kelley *et al.*, 2006], therefore do not appear necessary to explain the variation in primary magma temperatures in the Aleutians. On the other hand, SiO₂ concentrations increase with decreasing convergence rates (Figure 11b), indicating decreasing pressure of melt/mantle equilibration. As discussed above, this decrease in pressure with decreasing convergence rate is also consistent with the models (Figure 10) and is associated with a decrease in melt production.

[53] K₂O concentrations in arc lavas are higher in the western Aleutians than in the eastern Aleutians (Figure 11c). These values are significantly higher than typical mid-ocean ridge basalt (MORB) values suggesting that K₂O suggest a significant slab component [Plank and Langmuir, 1993]. On the basis of our models, we expect the extent of mantle melting, or F , to be lower in the western Aleutians than in the eastern Aleutians due to a combination of a lower convergence rate, which lowers temperatures along the melting front, and a steeper slab dip, which limits the width of the melting front. The signature of slab derived component is therefore expected to be more pronounced in the western Aleutians where less mantle melting occurs.

7.3. Melt Production Rate in the Aleutians

[54] Holbrook *et al.* [1999] and Lizarralde *et al.* [2002] estimated the magmatic flux along two seismic transects in the eastern Aleutians to be $\sim 67 \text{ km}^3 \text{ km}^{-1} \text{ Ma}^{-1}$. These estimates assume a uniform rate of crustal production over the lifetime of the convergent boundary. However, Stern and Bloomer [1992] found that for the Izu-Bonin-Mariana subduction zone, crust production rates were several times greater during the earliest stages of subduction than in mature arcs. Since no clear estimates exist on the fraction of crust produced in the early stages of subduction in the Aleutians, considerable uncertainty remains in using the volume of arc crust in estimating magmatic flux from ongoing subduction. The estimate of Holbrook *et al.* and Lizarralde *et al.* should therefore be viewed as upper bounds of the current crustal production rate.

[55] Our models predict a melt production of $\sim 19.1 \text{ km}^3 \text{ Ma}^{-1} (\text{arc km})^{-1}$ for a convergence rate similar to the average one in the Aleutians (60 km Ma^{-1}) and for a grain size of 1 mm. However, as grain size controls the flux of water into the melting region, and hence the melting rate, melt production in our models increases with increasing grain size. Therefore, for the same convergence rate and slab dip as above but with a uniform grain size of 10 mm, melt production increases from ~ 19.1 to $\sim 27.86 \text{ km}^3 \text{ Ma}^{-1} (\text{arc km})^{-1}$, a little under half the maximum melt production estimated above for the Aleutians. Furthermore, increasing the flux of water off the slab increases melt production rates. At a fixed grain size of 1 mm, increasing the flux of water off the slab by 200% leads to a melt production rate of $\sim 42 \text{ km}^3 \text{ Ma}^{-1} (\text{arc km})^{-1}$. If the grain size were increased to 10 mm, a lower flux of water would be needed to yield melt production rates similar to those found for the eastern Aleutians. It should also be noted that melt production in models such as ours are expected to be highly dependent on the melting relationships assumed. Small changes in the solidus or mantle temperatures would yield large increments in melt production.

[56] The current rate of crustal accretion, as indicated by the subaerial volumes of recent ($\leq 2 \text{ Ma}$) volcanic centers and the number of reported eruptions since 1700 at various locations along the Aleutians, is consistent with an eastward increase of melt production rate. Both the volume of the largest volcanoes and the number of eruptions increase to the east [Fournelle *et al.*, 1994]. Such an increase in intensity in the volcanic front may be related to the increase in melt production rates predicted with increasing convergence rates (Figure 6a).

7.4. Seismic Velocity Structure and Attenuation in the Wedge

[57] Seismic tomography studies of the mantle wedge have been reported for a number of convergent boundaries, although not for the Aleutians westward of the Alaskan Peninsula. Low seismic velocities and high attenuation reported in these studies are indicative of fluid and melt

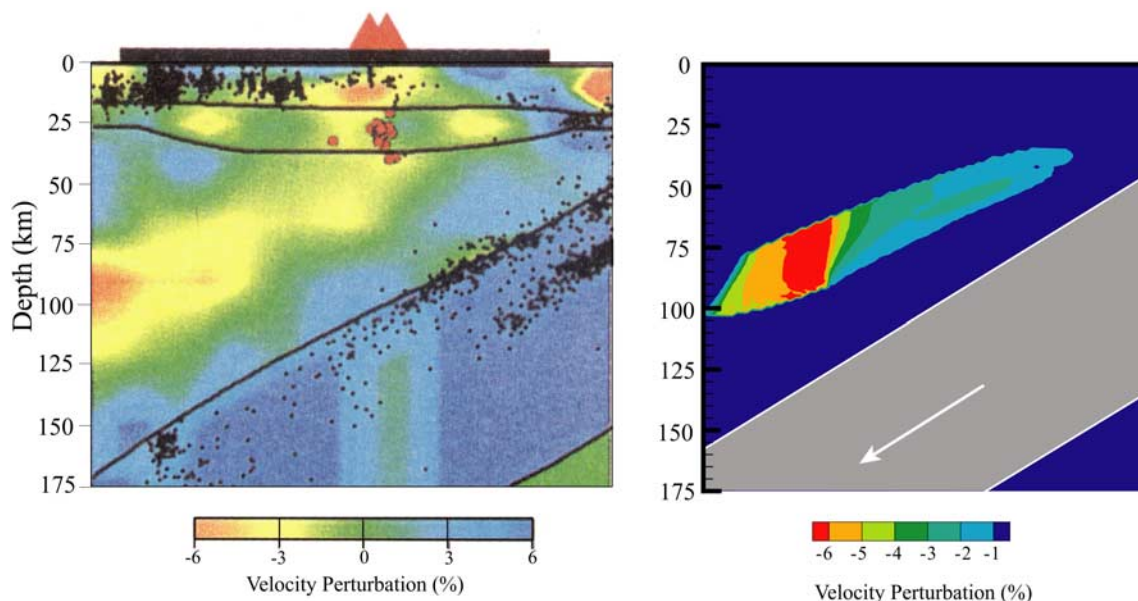


Figure 12. Predicted P wave velocity perturbation and attenuation from our models compared to the velocity perturbation results from *Nakajima et al.* [2001, slice FF in Plate 2]. Calculated velocity perturbations are attributed to anomalous temperatures and the presence of melt [*Hammond and Humphreys*, 2000] (see text for details).

distributions in the mantle wedge at subduction zones. For example, beneath the well-studied northeastern Japan, low V_P , low V_S and high V_P/V_S are distributed along the volcanic front in the uppermost mantle and extend downward to the back-arc side parallel to the slab [*Nakajima et al.*, 2001]. V_P and V_S velocities anomalies up to 6% are interpreted to reflect the presence of cracks filled with $\sim 1\%$ volume percent melt. P wave attenuation (Q_P) structure beneath Japan has been studied by *Zhao et al.* [1994] and *Tsumura et al.* [2000] in regions near those of the *Nakajima et al.* [2001] study. Zones of low Q_P correlate well with zones of low velocities, particularly in the southern part of their study area. In the northern part, low Q_P (between 145 and 170) appears in isolated zones beneath arc volcanoes whereas low seismic velocity is continuously distributed almost parallel to the slab. Beneath the Alaska subduction zone, the mantle wedge is also highly attenuating ($Q_S \sim 100$ – 143 ; $Q_P \sim 143$ – 200), but attenuation in bulk modulus is negligible, suggesting thermally activated solid-state attenuation processes [*Stachnik et al.*, 2004]. The distribution of attenuation is generally similar in Japan and Alaska subduction zone.

[58] Temperature has an important effect on both the anharmonic and anelastic components of seismic wave velocities. The anharmonic variation of V_P and V_S with temperature at upper mantle pressures is relatively well known compared to anelastic variation. *Karato* [1993, Table 1] gives values for the combined effect of anharmonic and anelastic effects as a function of attenuation. For levels of attenuation observed in the mantle wedge, anelastic effects on seismic velocity may be comparable to anharmonic effects. In our models we calculated Q_S from the combined effects of temperature and hydroxyl defect concentration from *Karato* [2003, Figure 2] and Q_P from $Q_P^{-1} = \frac{4}{9}Q_S^{-1}$.

The values of Q thus obtained are used to estimate the anelastic effect of temperature on seismic velocity. The resulting Q_P values agree reasonably well with values obtained by *Tsumura et al.* [2000] for the northeastern Japan and by *Stachnik et al.* [2004] for the Alaska subduction zone.

[59] Melt as well as temperature influence seismic velocities (see above discussion for observed perturbations at subduction zones). The effect of melt on seismic velocity and attenuation depends very strongly on whether melt is distributed as films on grain faces or as tubes along grain edges. Faces are more likely to be wetted at large melt fractions $\phi > \phi_{\text{film}}$ (for example, *Hammond and Humphreys* [2000] take $\phi_{\text{film}} = 1\%$). To estimate the seismic velocity perturbations induced by melt and temperature, we used derivatives of seismic velocity with respect to temperature and melt fraction given by *Hammond and Humphreys* [2000, Table 2]. This approach yields velocity perturbations up to $\sim 7\%$ and 10% for V_P and V_S , respectively, which are distributed parallel to the slab in the region of melting (between 30 km to 110 km depth). These results broadly agree with those of *Nakajima et al.* [2001] (Figure 12). In our models, the region of lowest seismic velocity occurs at shallower depth than observed. This difference may be attributable to the presence of hydrous fluids or hydroxyl defects in mineral grains which has not been taken into account in the above calculations.

[60] The lack of seismic velocity variation directly above the slab both in the observed seismic velocities suggests that relatively little melt or fluid is present directly above the slab in the Japan subduction zone. A similar region is seen in the seismic velocities calculated from our models. Our models show that melt migrates vertically upward once it is generated (Figure 9). However, the migration of hydrous fluids from the slab to regions where the temperature is

Table 1. Estimates of the Ascent Time of Hydrous Fluids^a

	40 km Ma ⁻¹	60 km Ma ⁻¹	100 km Ma ⁻¹
<i>Hydrous Fluid Ascent Time</i>			
d = 1 mm	1.3–6.7	0.93–3.33	0.55–2.1
d = 10 mm		0.35–1.8	
3 × flux of water		0.47–1.03	
<i>Melt Residence Time</i>			
d = 1 mm	0.2–0.21	0.13–0.27	0.19–0.26
d = 10 mm		0.083–0.17	
3 × flux of water		0.2–0.25	

^aEstimates, in Ma, are from their release point on the slab to the bottom of the wet melting region and of the melt residence time in the wet melting region for a uniform 1 and 10 mm grain size and for the case where the flux of water off the slab was tripled at a grain size of 1 mm. The range of time corresponds to the time associated with the first fluid streamline (first estimate) and the last streamline (second estimate) to reach the melting region. Fluid ascent time is reduced by both increasing the grain size, which increases the permeability (equation (16)), and increasing convergence rates, which brings hot mantle material closer to slab. Melt residence time within the wet melting region is short in comparison and is independent of convergence rate. It is also not as largely affected by grain size variations due to the relatively large volume fraction of melt in the melting region.

above the wet solidus has an important influence on the subsequent distribution of melt in the wedge.

7.5. Implications for the Convergent Boundary Magmatic Structure

[61] The 2-D models like those presented above do not explain important, probably fundamental, characteristics of convergent plate boundaries. One example is the existence of sharp volcanic front and its magmatic segmentation in the along the strike direction has frequently been noted [Marsh, 1979; Tamura et al., 2001; Honda and Yoshida, 2005]. Hot, perhaps molten, “fingers” have been imaged to extend in the wedge in regions such as northeastern Japan where dense seismometers arrays allow for good seismic resolution [Tamura et al., 2001]. Quaternary volcanic lineations are present above these fingers which could be interpreted as localized channels which permit fluids to migrate from the slab and the wedge to the surface.

[62] Furthermore, models like ours with distributed porous flow predict long fluid migration times. The time of hydrous fluid ascent from its release by slab dehydration reactions to the bottom of the wet melting region along with melt residence time within the melting region from our models are presented in Table 1. The range of ascent times at each convergence rate correspond to different path lengths along fluid flow lines and reflect the influence of solid flow on the rise of buoyant fluid as illustrated by the grey flow lines in Figure 9. The shorter of the two times correspond to the leftmost edge of the fluid column. The longer times correspond to the last flow line to rise into the melting region. We find that the time needed for fluids to migrate from the slab to the melting region is the major fraction of the total fluid ascent time. However, the ascent time is long compared to that inferred from isotopic disequilibrium studies find that between 10 and 200 ka have elapsed since the addition of hydrous fluids to the wedge [Turner, 2002, and references therein] (Elliott et al. [1997] find 30 ka for the Marianas and Bourdon et al. [1999] cite 60 ka for Tonga).

[63] This discrepancy could be resolved by channelized flow along fingers as imaged in northeast Japan [Tamura et al., 2001]. These could be envisioned as vertical fluid migration through relatively thin vertical sheets perpendicular to the strike of the plate boundary. Each of these vertical sheets could be interpreted as a realization of our 2-D models in which the vertical flux of water is the flux off the top of the slab enhanced by the ratio of the thickness of these vertical slices to their along-strike spacing. The spacing of volcanoes along the volcanic front could correspond to the location of the vertical slices. This localization would significantly decrease fluid migration times.

[64] A number of previous studies have argued that volcanic front occurs at a location where the slab reaches 100–150 km [Gill, 1981; Tatsumi and Eggins, 1995], but England et al. [2004] and Syracuse and Abers [2006] find that volcanism is distributed over a much broader region. This region could correspond to the top of the melting region in our models, but this does not explain the sharpness of the volcanic front. A potential focusing mechanism is a sloping decompaction channel which would form beneath the impermeable boundary defined by the solidus at the top of the wedge (Figure 13). Such a decompaction boundary layer has already been discussed in the context of melt migration beneath spreading centers as a focusing mechanism for melt produced over a broad region to within a couple of kilometers of the spreading axis [Sparks and

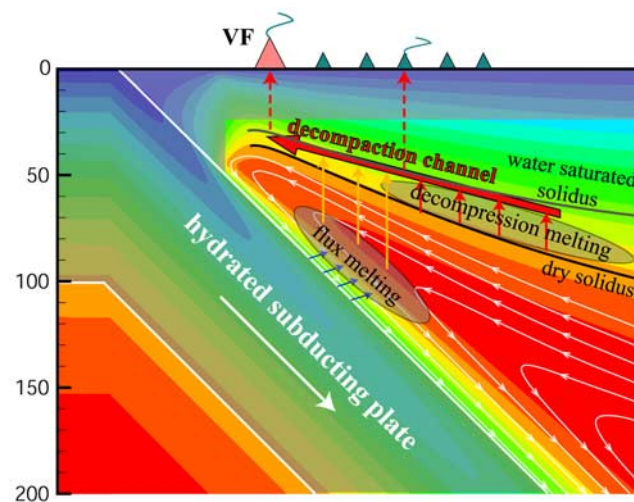


Figure 13. Schematic diagram of a melt generation and focusing. Melting occurs both by flux melting as water comes off the subducting slab and by adiabatic decompression as mantle entrained by the slab ascends into the wedge corner. Melt rises until it encounters a solid lid imposed by heat loss to the surface. Melt collects at this sloping impermeable boundary, in a layer of thickness determined by the compaction length, and buoyantly ascends to the shallowest point in the thermal structure, hypothesized to be the location of the volcanic front (VF). Both adiabatic decompression and wet melts intermingle in this layer, thereby yielding the observed compositional range of arc lavas. The wet solidus is from Grove et al. [2006], and the dry solidus was calculated as $1100^{\circ}\text{C} + 0.3 \times \text{depth}$.

Parmentier, 1991; Spiegelman, 1993] and may have been identified in the mantle section of the Oman ophiolite [Rabinowicz and Ceuleneer, 2005]. At subduction zones, buoyancy forces will cause melt in such a channel to migrate to the horizontal location where the relevant solidus reaches its shallowest depth. The accumulation of melt there could correspond to the location of the volcanic front. Both dry adiabatic decompression melts and flux-derived melts should be present in this channel in varying proportions. The intermingling of these melts may explain the compositional range and spatial distribution of volcanic compositions observed in arcs.

8. Conclusions

[65] Models of fluid migration and melting in the wedge above a subducting plate indicate that fluid released from the slab does not rise vertically but may be strongly influenced by solid flow in the wedge. Melting is localized to a region where hydrous fluids first encounter a region hot enough to melt and this is controlled by the effect of solid flow on fluid migration paths above the slab. Solid flow influences the extent of melting by determining the flux of fertile mantle material through this region. In contrast to decompression melting beneath spreading centers, the height of the melting column does not have a strong influence on the melt production rates. Melt production rates are sensitive to the pressure of melting and the maximum temperature along the melting front which vary with convergence rate. Small changes in mantle potential temperatures, or equivalently varying mantle fertility, also strongly influence melt production rates. The insight into wet melting processes gained from these models can be applied to subduction zones such as the Aleutians and may help identify and better understand the potential factors influencing fluid migration and melt production at convergent plate boundaries.

[66] The influence of solid flow may be even further enhanced in more realistic 3-D flow structure where fluid released by the slab may be focused into relatively thin vertical sheets along the strike of the convergent plate boundary, corresponding to the spacing of volcanic centers. A focusing mechanism, such as a decompression boundary layer beneath the lithosphere, is however still needed to focus melt produced over a broad region to the observed sharp volcanic front and to explain the compositional variation observed in arc volcanoes.

[67] **Acknowledgments.** We thank Tim Grove and Geoff Abers for their helpful and careful reviews of our manuscript. We are grateful to Alberto Saal and Peter Kelemen for enlightening conversations on geochemistry. Funding for this work was provided by NSF grant OCE-0242261.

References

- Aharonov, E., J. A. Whitehead, P. B. Kelemen, and M. Spiegelman (1995), Channeling instability of upwelling melt in the mantle, *J. Geophys. Res.*, *100*, 20,433–20,450.
- Ahern, J. L., and D. L. Turcotte (1979), Magma migration beneath an ocean ridge, *Earth Planet. Sci. Lett.*, *45*, 115–122.
- Arcay, D., E. Tric, and M. P. Doin (2005), Numerical simulations of subduction zones; effect of slab dehydration on the mantle wedge dynamics, *Phys. Earth Planet. Inter.*, *149*, 1–2, 133–153.
- Asimow, P. D., J. E. Dixon, and C. H. Langmuir (2004), A hydrous melting and fractionation model for mid-ocean ridge basalts: Application to the Mid-Atlantic Ridge near the Azores, *Geochem. Geophys. Geosyst.*, *5*, Q01E16, doi:10.1029/2003GC000568.
- Audétat, A., and H. Keppler (2004), Viscosity of fluids in subduction zones, *Science*, *303*, 513–516.
- Baker, J. L., C. E. Hall, P. D. Asimow, P. Smith, and M. Gurnis (2004), Subduction dynamics and mass transfer: A synthesis model, *Eos Trans. AGU*, *85*(47), Fall Meet. Suppl., Abstract V12A-08.
- Barckhausen, U., C. R. Ranero, R. von Huene, S. C. Cande, and H. A. Roeser (2001), Revised tectonic boundaries in the Cocos plate off Costa Rica: Implications for the segmentation of the convergent margin and for plate tectonic models, *J. Geophys. Res.*, *106*, 19,207–219,220.
- Bell, D. R., G. R. Rossman, J. Maldener, D. Endisch, and F. Rauch (2003), Hydroxide in olivine: A quantitative determination of the absolute amount and calibration of the IR spectrum, *J. Geophys. Res.*, *108*(B2), 2105, doi:10.1029/2001JB000679.
- Billen, M. L., and M. Gurnis (2001), A low viscosity wedge in subduction zones, *Earth Planet. Sci. Lett.*, *193*, 227–236.
- Bourdon, B., S. Turner, and C. Allegre (1999), Melting dynamics beneath the Tonga-Kermadec island arc inferred from ²³¹Pa-²³⁵U systematics, *Science*, *286*, 2491–2493.
- Cagnioncle, A.-M., and E. M. Parmentier (2006), The effect of peridotite serpentinization on solid slow and thermal distributions in the wedge above a subducting slab, *Eos Trans. AGU*, *87*(52), Fall Meet. Suppl., Abstract T22C-01.
- Conder, J. A., D. A. Wiens, and J. Morris (2002), On the decompression melting structure at volcanic arcs and back-arc spreading centers, *Geophys. Res. Lett.*, *29*(15), 1727, doi:10.1029/2002GL015390.
- Davies, J. H., and D. J. Stevenson (1992), Physical model of source region of subduction zone volcanics, *J. Geophys. Res.*, *97*, 2037–2070.
- Eberle, M. A., O. Grasset, and C. Sotin (2002), A numerical study of the interaction between the mantle wedge, subducting slab, and overriding plate, *Phys. Earth Planet. Inter.*, *134*, 191–202.
- Elliott, T., T. Plank, A. Zindler, W. White, and B. Bourdon (1997), Element transport from slab to volcanic front at the Mariana Arc, *J. Geophys. Res.*, *102*, 14,991–15,019.
- England, P., R. Engdahl, and W. Thatcher (2004), Systematic variation in the depths of slabs beneath arc volcanoes, *Geophys. J. Int.*, *156*, 377–408.
- Fournelle, J. H., B. D. Marsh, and J. D. Myers (1994), Age, character, and significance of Aleutians arc volcanism, in *The Geology of Alaska*, vol. G-1, *The Geology of North America*, edited by G. Plafker and H. C. Berg, pp. 723–757, Geol. Soc. of Am., Boulder, Colo.
- Gaetani, G. A., and T. L. Grove (1998), The influence of water on melting of mantle peridotite, *Contrib. Mineral. Petrol.*, *131*, 323–346.
- Gerya, T. V., and D. A. Yuen (2003), Rayleigh-Taylor instabilities from hydration and melting propel “cold plumes” at subduction zones, *Earth Planet. Sci. Lett.*, *212*, 47–62.
- Gill, J. (1981), *Orogenic Andesites and Plate Tectonics*, 390 pp., Springer, New York.
- Grove, T. L., L. T. Elkins-Tanton, S. W. Parman, N. Chatterjee, O. Müntener, and G. A. Gaetani (2003), Fractional crystallization and mantle-melting controls on calc-alkaline differentiation trends, *Contrib. Mineral. Petrol.*, *145*, 515–533.
- Grove, T. L., N. Chatterjee, S. W. Parman, and E. Medard (2006), The influence of H₂O on mantle wedge melting, *Earth Planet. Sci. Lett.*, *249*, 74–89.
- Hammond, W. C., and E. D. Humphreys (2000), Upper mantle seismic wave attenuation; effects of realistic partial melt distribution, *J. Geophys. Res.*, *105*, 10,987–10,999.
- Hirschmann, M. M., P. D. Asimow, M. S. Ghiorso, and E. M. Stöpler (1999), Calculation of peridotite partial melting from thermodynamic models of minerals and melts; II, Isobaric variations in melts near the solidus and owing to variable source composition, *J. Petrol.*, *40*, 297–313.
- Hirth, G., and D. L. Kohlstedt (2003), Rheology of the upper mantle and the mantle wedge: A view from the experimentalists, in *Inside the Subduction Factory*, *Geophys. Monogr. Ser.*, vol. 138, edited by J. M. Eiler, pp. 293–309, AGU, Washington, D. C.
- Holbrook, W. S., D. Lizarralde, S. McGeary, N. L. Bangs, and J. B. Diebold (1999), Structure and composition of the Aleutian island arc and implications for continental growth, *Geology*, *27*, 32–42.
- Holtzman, B. K., and D. L. Kohlstedt (2003), Melt segregation and strain partitioning: implications for seismic anisotropy and mantle flow, *Science*, *301*, 1227–1230.
- Honda, S., and T. Yoshida (2005), Application of the model of small-scale convection under the island arc to the NE Honshu subduction zone, *Geochem. Geophys. Geosyst.*, *6*, Q01002, doi:10.1029/2004GC000785.
- Iwamori, H. (1998), Transportation of H₂O and melting in subduction zones, *Earth Planet. Sci. Lett.*, *160*, 65–80.

- Karato, S. (1993), Importance of anelasticity in the interpretation of seismic tomography, *Geophys. Res. Lett.*, *20*, 1623–1626.
- Karato, S. (2003), Mapping water in the upper mantle, in *Inside the Subduction Factory*, *Geophys. Monogr. Ser.*, vol. 138, edited by J. M. Eiler, pp. 135–152, AGU, Washington, D. C.
- Katz, R. F., M. Spiegelman, and C. H. Langmuir (2003), A new parameterization of hydrous mantle melting, *Geochem. Geophys. Geosyst.*, *4*(9), 1073, doi:10.1029/2002GC000433.
- Kay, S. M., and R. W. Kay (1994), Aleutian magmas in space and time, in *The Geology of North America*, vol. G-1, *The Geology of Alaska*, edited by G. Plafker and H. C. Berg, pp. 687–722, Geol. Soc. of Am., Boulder, Colo.
- Kelemen, P. B., J. L. Rilling, E. M. Parmentier, L. Mehl, and B. R. Hacker (2003a), Thermal structure due to solid-state flow in the mantle wedge beneath arcs, in *Inside the Subduction Factory*, *Geophys. Monogr. Ser.*, vol. 138, edited by J. M. Eiler, pp. 293–309, AGU, Washington, D. C.
- Kelemen, P. B., et al. (2003b), Along-strike variation in the Aleutians island arc: Genesis of high Mg # andesite and implications for continental crust, in *Inside the Subduction Factory*, *Geophys. Monogr. Ser.*, vol. 138, edited by J. M. Eiler, pp. 223–272, AGU, Washington, D. C.
- Kelley, K. A., T. Plank, T. L. Grove, E. M. Stolper, S. Newman, and E. Hauri (2006), Mantle melting as a function of water content beneath back-arc basins, *J. Geophys. Res.*, *111*, B09208, doi:10.1029/2005JB003732.
- Lizarralde, D., W. S. Holbrook, S. McGeary, N. L. Bangs, and J. B. Diebold (2002), Crustal construction of a volcanic arc, wide-angle seismic results from the western Alaska Peninsula, *J. Geophys. Res.*, *107*(B8), 2164, doi:10.1029/2001JB000230.
- Marsh, B. D. (1979), Island arc development; some observations, experiments, and speculations, *J. Geol.*, *87*, 687–713.
- McKenzie, D. (1984), The generation and compaction of partially molten rock, *J. Petrol.*, *25*, 713–765.
- Mibe, K., T. Fujii, and A. Yasuda (1999), Control of the location of the volcanic front in island arcs by aqueous fluid connectivity in the mantle wedge, *Nature*, *401*, 259–262.
- Morris, J., and S. R. Hart (1983), Isotopic and incompatible element constraints on the genesis of island arc volcanics from Cold Bay and Amak Island, Aleutians, and implications for mantle structure, *Geochim. Cosmochim. Acta*, *47*, 2015–2030.
- Myers, J. D., B. D. Marsh, and A. K. Sinha (1985), Strontium isotopic and selected trace element variations between two Aleutian volcanic centers (Adak and Atka): Implications for the development of arc volcanic plumbing systems, *Contrib. Mineral. Petrol.*, *91*, 221–234.
- Nakajima, J., T. Matsuzawa, A. Hasegawa, and D. Zhao (2001), Three-dimensional structure of V_p , V_s , and V_p/V_s beneath northeastern Japan: Implications for arc magmatism and fluids, *J. Geophys. Res.*, *106*, 21,843–821,857.
- Pawley, A. R. (2003), Chlorite stability in mantle peridotite: The reaction clinocllore + enstatite = forsterite + pyrope + H₂O, *Contrib. Mineral. Petrol.*, *144*, 449–456.
- Pawley, A. R., and J. R. Holloway (1993), Water sources for subduction zone volcanism: New experimental constraints, *Science*, *260*, 664–667.
- Phipps Morgan, J. (1987), Melt migration beneath mid-ocean spreading centers, *Geophys. Res. Lett.*, *14*, 1238–1241.
- Plank, T., and C. H. Langmuir (1993), Tracing trace elements from sediment input to volcanic output at subduction zones, *Nature*, *362*, 739–743.
- Rabinowicz, M., and G. Ceuleneer (2005), The effect of sloped isotherms on melt flow in the shallow mantle: A physical and numerical model based on observations in the Oman ophiolite, *Earth Planet. Sci. Lett.*, *229*, 231–246.
- Rüpke, L. H., M. J. Phipps, M. Hort, and J. A. D. Connolly (2002), Are the regional variations in Central American arc lavas due to differing basaltic versus perioditic slab sources?, *Geology*, *30*, 1035–1038.
- Schmidt, M. W., and S. Poli (1998), Experimentally based water budgets for dehydrating slabs and consequences for arc magma generation, *Earth Planet. Sci. Lett.*, *163*, 361–379.
- Scott, D. R., and D. J. Stevenson (1984), Magma ascent by porous flow, *J. Geophys. Res.*, *91*, 9283–9296.
- Sleep, N. H. (1974), Segregation of magma from a mostly crystalline mush, *Geol. Soc. Am. Bull.*, *85*, 1222–1242.
- Smolakiewicz, P. K. (1983), A fully multidimensional positive definite advection transport algorithm with small implicit diffusion, *J. Comput. Phys.*, *54*, 325–362.
- Sparks, D. W., and E. M. Parmentier (1991), Melt extraction from the mantle beneath spreading centers, *Earth Planet. Sci. Lett.*, *105*, 368–377.
- Spiegelman, M. (1993), Physics of melt extraction: Theory, implications and applications, *Philos. Trans. R. Soc. London*, *342*, 23–41.
- Spiegelman, M., and D. McKenzie (1987), Simple 2-D models for melt extraction at mid-ocean ridges and island arcs, *Earth Planet. Sci. Lett.*, *83*, 137–152.
- Stachnik, J. C., G. A. Abers, and D. H. Christensen (2004), Seismic attenuation and mantle wedge temperatures in the Alaska subduction zone, *J. Geophys. Res.*, *109*, B10304, doi:10.1029/2004JB003018.
- Stern, R. J., and S. H. Bloomer (1992), Subduction zone infancy: Examples from the Eocene Izu-Bonin-Mariana and Jurassic California arcs, *Geol. Soc. Am. Bull.*, *104*, 1621–1636.
- Syracuse, E. M., and G. A. Abers (2006), Global compilation of variations in slab depth beneath arc volcanoes and implications, *Geochem. Geophys. Geosyst.*, *7*, Q05017, doi:10.1029/2005GC001045.
- Tackley, P. J., and S. D. King (2003), Testing the tracer ratio method for modeling active compositional fields in mantle convection simulations, *Geochem. Geophys. Geosyst.*, *4*(4), 8302, doi:10.1029/2001GC000214.
- Tamura, Y., Y. Tatsumi, D. Zhao, Y. Kido, and H. Shukuno (2001), Hot fingers in the mantle wedge: New insights into magma genesis in subduction zones, *Earth Planet. Sci. Lett.*, *197*, 105–116.
- Tatsumi, Y., and S. Eggins (1995), *Subduction Zone Volcanism*, 211 pp., Blackwell Sci., Malden, Mass.
- Tsumura, N., S. Matsumoto, S. Horiuchi, and A. Hasegawa (2000), Three-dimensional attenuation structure beneath the northeastern Japan arc estimated from spectra of small earthquakes, *Tectonophysics*, *319*, 241–260.
- Turner, S. P. (2002), On the time-scales of magmatism at island-arc volcanoes, *Philos. Trans. R. Soc. London*, *360*, 2853–2871.
- van Barga, N., and H. S. Waff (1986), Permeabilities, interfacial areas, and computations of equilibrium microstructures, *J. Geophys. Res.*, *91*, 9261–9276.
- van der Waal, D., P. Chopra, M. Drury, and G. J. Fitz (1993), Relationships between dynamically recrystallized grain size and deformation conditions in experimentally deformed olivine rocks, *Geophys. Res. Lett.*, *20*, 1479–1482.
- van Keken, P. E., B. Kiefer, and S. M. Peacock (2002), High-resolution models of subduction zones: Implications for mineral dehydration reactions and the transport of water into the deep mantle, *Geochem. Geophys. Geosyst.*, *3*(10), 1056, doi:10.1029/2001GC000256.
- von Huene, R., C. R. Ranero, R. Weinrebe, and W. Hinz (2000), Quaternary convergent margin tectonics of Costa Rica, segmentation of the Cocos Plate, and Central American volcanism, *Tectonics*, *19*, 314–334.
- Wark, D. A., and E. B. Watson (1998), Grain-scale permeabilities of texturally equilibrated, monomineralic rocks, *Earth Planet. Sci. Lett.*, *164*, 591–605.
- Wark, D. A., C. A. Williams, E. B. Watson, and J. D. Price (2003), Re-assessment of pore shapes in microstructurally equilibrated rocks, with implications for permeability of the upper mantle, *J. Geophys. Res.*, *108*(B1), 2050, doi:10.1029/2001JB001575.
- Wiens, D. A., K. A. Kelley, and T. Plank (2006), Mantle temperature variations beneath back-arc spreading centers inferred from seismology, petrology, and bathymetry, *Earth Planet. Sci. Lett.*, *248*, 30–42.
- Wiggins, C., and M. Spiegelman (1995), Magma migration and magmatic solitary waves in 3-D, *Geophys. Res. Lett.*, *22*, 1289–1292.
- Zhao, D., A. Hasegawa, and H. Kanamori (1994), Deep structure of Japan subduction zone as derived from local, regional, and teleseismic events, *J. Geophys. Res.*, *99*, 22,313–322,329.
- Zhu, W., and G. Hirth (2003), A network model for permeability in partially molten rocks, *Earth Planet. Sci. Lett.*, *212*, 407–416.
- Zimmerman, M. E., S. Shuqing, D. L. Kohlstedt, and S. Karato (1999), Melt distribution in mantle rocks deformed in shear, *Geophys. Res. Lett.*, *26*, 1505–1508.

A.-M. Cagnioncle and E. M. Parmentier, Department of Geological Sciences, Brown University, Box 1846, Providence, RI 02912, USA. (amandine@brown.edu)

L. T. Elkins-Tanton, Department of Earth, Atmospheric and Planetary Sciences, Massachusetts Institute of Technology, 77 Massachusetts Avenue, Cambridge, MA 02139-4307, USA.